Carbon supported aluminium trifluoride nanoparticles functionalized lithium manganese oxide for the development of advanced lithium ion battery system

By

Shane Willenberg

(BSc Honours)

A mini-thesis submitted in partial fulfilment of the requirements for the degree of
Magister Scientiae in Nanoscience
Faculty of Science
University of the Western Cape
Cape Town / South Africa
Supervisor: Dr. Natasha Ross
Co-supervisor: Prof. Emmanuel Iwuoha

December 2017

Declaration

I hereby declare that "**Carbon supported aluminium trifluoride nanoparticles functionalized lithium manganese oxide for the development of advanced lithium ion battery system**" is my own work and it has not been submitted before for any degree or examination in any other university, and all the sources I have used or quoted have been indicated or acknowledged by way of complete references.

Shane Willenberg:

 Signed: Date: 15-12-17

UNIVERSITY *of the*
WESTERN CAPE

i

Abstract

A novel lithium ion (Li-ion) battery cathode material has been investigated for potential mobile technology energy storage applications. I have successfully synthesized Lithium Manganese oxide (LMO), reduced Graphene Oxide (rGO) and Aluminium trifluoride (AlF_3). The cathode coated nanocomposite was compiled of the aforementioned materials to give [$AlF_3LiMn_2O_4$-rGO]. A single-phase spinel was observed from X-ray diffraction (XRD) studies with a high intensity (111) plane which indicates good electrochemical activity. No alterations to the crystal structure were observed after forming the composite nano-cathode material. Fourier transfer infrared (FTIR) spectroscopy showed the vibrational spectrum of $LiMn_2O_4$ with a with asymmetric MnO_6 stretching confirming that the spinel was formed. The A^{1g} mode of Raman spectroscopy showed Mn-O vibrations. From High-Resolution Transmission Electron Microscopy (HRTEM) we confirmed a highly crystalline material with separation (d-spacings) calculated as 0.187 nm. This could also be said for AlF_3 and rGO with similar d-spacings in the (Å) angstrom range. HRTEM allows us to deduce that the [$AlF_3LiMn_2O_4$-rGO] nanocomposite cathode material will display improved lithium diffusion properties, as the Li^+ pathlength is shorter for the charge/discharge process. High Resolution Scanning Electron Microscopy (HRSEM) showed impressive spinel growth of the AlF_3 coated nanocomposite cathode material. The characterization results for [$AlF_3LiMn_2O_4$-rGO] cathode material hints that a structurally and electrochemically stable novel coated lithium ion cathode has been synthesized and can potentially be employed as a cathode material in new age lithium ion batteries. The current conducting capacity improved by about 5 times as can be seen when comparing the peak current densities from 2.89 µA and -2.08 µA to 10.14 µA and -7.17 µA, clearly hinting towards improved electrochemical capacities and energy densities of the novel [$AlF_3LiMn_2O_4$-rGO] nanocomposite cathode material when applied to a battery which gives it an extended lifespan.

Acknowledgements

All praise, glory and honour to God for giving me the strength and courage to complete my MSc thesis.

I am also thankful for my supervisor, Dr. Natasha Ross, for her guidance and expertise in the field of energy storage devices. I'm also thankful Prof. Emanuel Iwuoha for his wisdom and affording me the opportunity to be part of the SensorLab research group.

To my parents, and brothers, thank you all for your encouraging support and prayers.

To the Department of Chemistry staff especially Prof P. Baker, Dr F. Ajayi, Dr T. Waryo, Dr. Masikini, Prof. Jahed and all the MSc Nanoscience lecturers who travelled vast distances across the world to share their knowledge thank you all so much. Special thanks to Mrs. W. Jackson, for your assistance and support.

My appreciation also goes to Sensor Lab senior researchers and colleagues especially Ntuthuko Wonderboy, Miranda Ndipingwe, Dr. Lindsay Wilson, Dr. Francis Muya, Dr. Meryk Ward, Dr. Unathi Sidwaba, Dr. Keagan Pogpas, Zolani Myalo, Earl McDonald, Danielle Sass and all my Nanoscience colleagues. Thank you all for your great help, support and friendship. You have truly made my work much easier. I will also like to thank the Nanoscience and Nanotechnology Postgraduate Teaching and Training Platform (NNPTTP) especially Mrs. V. Jamalie and Mrs. C. Abrahams for their constant help and support as well as the Department of Science and Technology for awarding me the MSc Nanoscience scholarship.

i.   Table of Contents

List of Figures

v

UNIVERSITY *of the*

WESTERN CAPE

Chapter1: Introduction

Chapter Overview

This chapter highlights that fact that sustainable renewable energy resources are needed to meet the requirements for the global energy demand. These energy sources are to be coupled with energy storage systems such as batteries which are capable of storing energy and discharging stored energy when required

1.1 World energy crisis

The current global energy demand exceeds the earths energy resources. The earth's energy resources are therefore not sustainable as it will not meet the energy requirements of the future. This crisis is primarily due to the rapidly increasing global population and the evolution of technological devices which require large amounts of energy [1]. These devices include cell phones, laptops, electric vehicles and many others which need to be charged up at all times in this era we call the age of technology.

Fossil fuels have been used since the beginning of time. It was only during the industrial revolution in the 18th century that the extraction of coal and oil became a wide spread necessity in order to fuel power tools and machines. A little over 200 years on, mankind is superseding these essential fossil fuels as a result of overconsumption. It is estimated that oil reserves would have depleted by the year 2050 [2], this can be observed in Figure 1 below. Coal and gas will also run towards completion very soon after oil, this is due to the energy fuel gap which will be created.

1
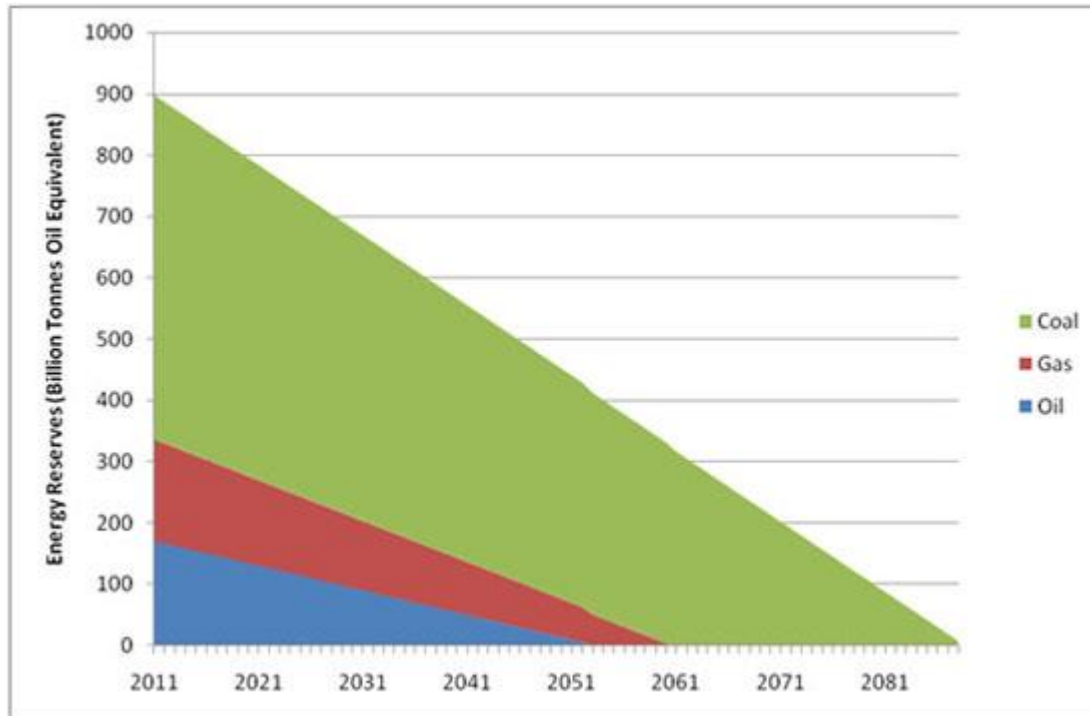
Figure 1: Global energy reserves and expected depletion dates [2]

Fossil fuels are running low and therefore renewable sustainable energy sources are required. The use of fossil fuels also has a negative impact on the environment [3]. Combustion of fossil fuels is one of the major contributing factors to global warming as the process of burning fossil fuels in order to generate electrical energy produces high volumes of carbon dioxide (CO_2). It is estimated that the amount of CO_2 produced from the motor industry will increase by 65% in the year 2020. This is due to the 1.5 billion vehicles which are expected to be on roads across the world [4].

Sustainable energy is defined as the fulfillment of energy for our current requirements and meeting the energy requirements for future generations to come. Renewable energy sources are generally more environmentally friendly, cheaper and are considered green energy sources. These sources are mainly solar, hydro, biomass and wind energy to name a few [5]–[7]. The use of these renewable energy sources will be unsustainable in various parts of the world due to seasonal weather patterns. In order to obtain maximum efficiency from these renewable energy sources, we need energy storage devices which are able to reproduce the electrical energy stored at a moment's notice. It is for this reason that I have decided to study energy storage devices, more specifically batteries.

1.2   Batteries

Batteries are energy storage devices which convert chemical energy into electrical energy by means of a redox reaction. A battery is composed of two or more electrochemical cells. These electrochemical cells are connected in series or parallel in order to create the desired voltage or power output. Primary batteries can only be used once and secondary batteries are rechargeable. Primary batteries cannot be recharged due to the nature of its electrolyte; there is no liquid electrolyte. It is thus given the term dry cell. These batteries have a high-energy density and are used in smaller portable electronic applications such as in flash torches and cameras. The rechargeable property which the secondary battery contains, is very attractive to many applications. These include mobile phones, laptops and electric vehicles. This is because the battery is able to restore a full 100% charge after being discharged. During discharge, electrons flow from the anode to the cathode. The charge process is the exact opposite of discharging where electrons are transported from the cathode to the anode through the external electrical circuit and ions migrate from the cathode to anode through the electrolyte [8]. An example of the discharging redox process of a $ZnCl_2$ electrochemical cell can be observed below:

$$\text{Anode: } Zn^0 \rightarrow Zn^{2+} + 2e^- \tag{1}$$

$$\text{Cathode: } Cl_2 + 2e^- \rightarrow 2Cl^- \tag{2}$$

$$\text{Overall: } Zn^0 + Cl_2 \rightarrow Zn^{2+} + 2Cl^- \tag{3}$$

The primary components of a battery include the anode, cathode and electrolyte. The cathode is the positive electrode and the anode is the negative electrode. The electrolyte controls the flow of positive ions, usually lithium ions from one electrode to the other. Electrons do not flow through the electrolyte but rather through the external electrical circuit. Current collectors at the anode and

3

cathode allow for the migration of electrons to take place. Copper metal is usually used at the anode and aluminum at the cathode. Both electrodes are complex composites which contain polymeric binder material to hold them in place [9]. The current global market for batteries is $132 billion with demand increasing at a rapid rate in countries such as India, Japan and South Korea [10].

1.3   Battery Concepts

A battery is composed of a group of electrochemical cells which are packed together to form a battery. Inside a cell, there are three components namely; anode, cathode and electrolyte. The anode is the negative electrode and is the site at which oxidation takes place. The cathode is the positive electrode and is the site at which reduction takes place. The electrolyte is the medium through which ions are transported in-between electrodes. In ideal cell conditions, the electrolyte will not participate in cell reactions. Thermodynamics and kinetics play an important role in determining the energy storage and power characteristics of a battery. The basic thermodynamic considerations for reversible electrochemical systems follow below:

$$\Delta G \ = \ \Delta H \ - \ T\Delta S \tag{4}$$

and

$$\Delta G° \ = \ \Delta H° \ - \ T\Delta S° \tag{5}$$

ΔG is the change in Gibbs free energy or the energy of a reaction available for useful work. ΔH is the change enthalpy or the energy released by the reaction. ΔS is the change in entropy and T is the absolute temperature. $T\Delta S$ is the heat associated with the organisation/disorganization of the materials. $\Delta G°$, $\Delta H°$ and $\Delta S°$ are the Gibbs free energy, Enthalpy and Entropy at standard conditions, 25ºC. The change in the standard free energy of a cell reaction is the driving force which enables a battery to deliver electrical energy to an appliance. Consider the cell reaction below:

$$Li_xMn_2O_4 + Li_yC_6 \rightarrow Li_{x+\delta}Mn_2O_4 + Li_{y-\delta}C_6 \tag{6}$$

4

The thermodynamic quantity describing the change in enrgy as a function of Li concentration in the chemical potential (μ) defined as:

$$\mu = \frac{\delta G}{\delta x} \tag{7}$$

Where x is the number of inserted Li atoms. The change in free energy can be expressed as;

$$\Delta G = -nFE \tag{8}$$

Where n is the number of electrons in both electrode reactions. F is Faradays constant and E is the potential difference between the electrodes.

In order to understand the relationship between chemical and electrical energy in a battery system, we combine equations 7 and 8 as follows;

$$\partial FE = \mu a - \mu a \tag{9}$$

Where μa and μa are the chemical potentials of Li ions in the cathode and anode.

The current flowing through the external circuit can be defined as the charge per unit time and is given as; $I = Q/t$. Where I (A) is the current in Amperes, Q (C) is the charge in Coulombs and t (s) is the time in seconds. The applied charge will consume reactant according to its redox constituents [11]. This is given by

$$Nm = \frac{It}{n\,N_A\,e} = \frac{It}{nF} \tag{10}$$

Where n is the number of electrons gained or lost, N_A is Avogadro's constant, e is the charge on the electron and F is Faraday's constant.

In a cell, redox reactions occur at the electrode/electrolyte interface. These reactions are referred to as the charge transfer process. The current flow across the electrode is equivalent to the amount of redox reactions taking place. The rate of current flow is given by the Butler-Volmer equation below [11]:

5

$$\mathrm{logi_o} = \log(\mathrm{nFA}k^0) + (1-a)\log[\mathrm{Ox}]^{\mathrm{bulk}} + a\log[\mathrm{Red}]^{\mathrm{bulk}} \qquad (11)$$

1.3.1   Fuel Cells

Fuel cells (FC) serve as a source of clean power generation, contributing zero greenhouse emissions to the environment. This is due to the fact that fuel cells convert hydrogen and oxygen into steam as a waste product. Similar to batteries, FC are very quiet in application. FC have been found to be more efficient in converting energy in a fuel to power than in gasoline engines or utility thermal plants. Fuel cells can be incorporated into all areas of society. These include utilities, car manufacturers and in portable electronic devices such as laptops. Governments around the world have realized the need for alternative power sources and are investing capital into FC research and development in order to move away from fossil fuels as they are depleting and have an ever-increasing carbon footprint.

FC convert chemical energy into electrical energy. FC are composed of an anode, cathode and electrolyte which is the medium for ionic transport within the FC. Unlike batteries, FC do not contain the fuel and oxidant within the FC but are supplied by an external fuel source. FC are similar to internal combustion engines, they operate as long as there is a constant fuel supply. In FC hydrogen serves as the fuel source and water vapour escapes from the exhaust. Fuels such as methanol and methane must be converted to hydrogen in order to be used in FC. The basic reaction which takes place in a H_2-O_2 FC is as follows:

$$H_2 + \frac{1}{2}O_2 \rightarrow H_2O \qquad\qquad E^o = 1.229 \text{ V} \qquad (12)$$
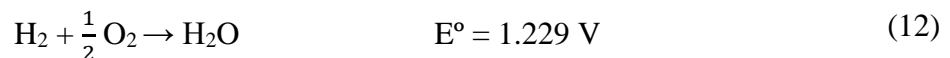
Electrical energy is obtained by the conversion of chemical energy due to the reaction between hydrogen and oxygen at the electrodes in the FC. Low temperature FC use acidic or alkaline electrolytes. The electrode reaction in acidic electrolytes are as follows:

$$\text{Anode: } H_2 + 2e^- \rightarrow 2H^+ \tag{13}$$

$$\text{Cathode: } O_2 + 2H^+ + 2e^- \rightarrow H_2O_2 \tag{14}$$

$$H_2O_2 + 2H^+ + 2e^- \rightarrow 2H_2O \tag{15}$$

$$\text{Overall: } O_2 + 4H^+ + 4e^- \rightarrow 2H_2O \tag{16}$$
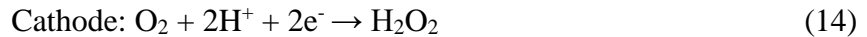
Catalysts are required to speed up the dissociation rate of H_2 at the anode. These include platinum-based alloys which is also used at the cathode in order to improve reaction rate. This platinum based catalysts are very expensive and are thus modified on nanostructured dimensions with various compositions of porous in order to enhance its properties and lower the product cost price [12]. Governments around the world are funding FC research due to the need for sustainable renewable energy. The current FC investment market value amounts to \$140 million [13].

1.4 Electrochemical Storage Devices

An Electrochemical Capacitor (EC) is a device which stores charge. The standard configuration of an EC is two conductors which have equal but opposite charges. EC can be used in various power utility applications such as the storage of electrochemical energy, filtering out unwanted frequency signals and making frequency dependent and independent voltage divides when combined with resistors. EC can also be incorporated into hybrid and electric vehicles. The global market for EC products and applications is between \$150 and \$200 million annually.

EC are composed of electric double layer and pseudo capacitors. EC differ from conventional dielectric and electrolytic capacitors in that they store more energy. The electrochemical storage properties of EC include rapid charging, reliability, high cyclability and a wide range of safe

7

operation temperatures. Repetitive processes such as applying of brakes in cars or the descent in elevators allow for easy energy generation in EC. Large scale EC are able to regulate the power of the electrical grid so as to prevent shutdowns and power outages. EC differ to batteries in that they store electrical charge instead of chemical energy. Due to the fact that electrical energy is stored physically, there is very little charge-discharge limitations and can undergo millions of cycles before failure. EC are thus also able to deliver more power than batteries. The basic operation of EC can be seen in the circuit diagram below:
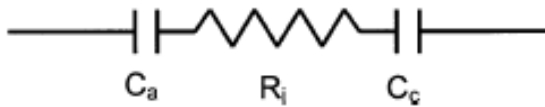
Figure 2: Basic operation of EC

C_a and C_c are the double layer capacitances of the anode and cathode. R_i is the internal resistance.

The annual market for EC is \$150 - \$200 million. The Ragone in Figure 3 plot below shows the comparison between batteries, FC capacitors and supercapacitors in terms of their specific power and energy densities. It is observed that batteries have the more stable power to energy conversion than FC and capacitors, as FC have a high-energy density and capacitors/supercapacitors have high power densities. Batteries are also cheap and have a minimum impact on the environment. It is for this reason that batteries are far more commercialized than any of its energy storage competitors.
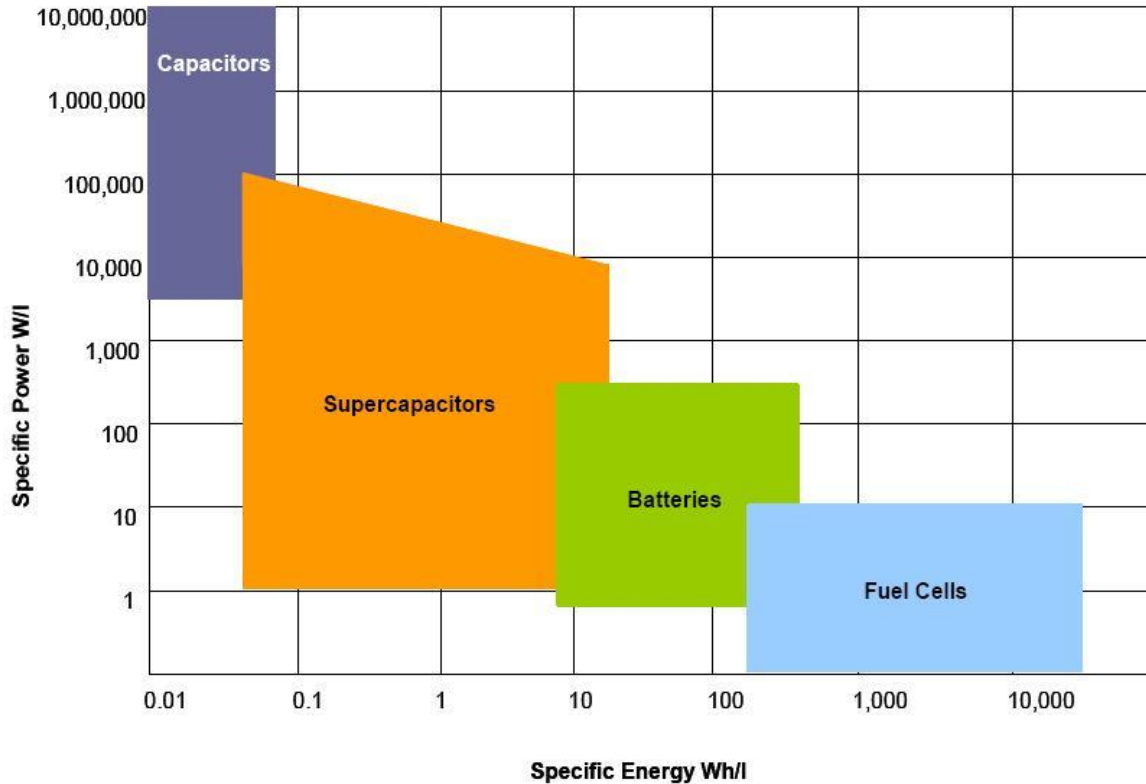
Figure 3: Power density as a function of energy density for various energy storage devices [12]

1.5   Classification of batteries

Batteries can be classified as three types namely; primary, reserve and secondary. Primary batteries are non-rechargeable and must be thrown away after use. Reserve batteries are similar to primary batteries in that they are not rechargeable. They usually have a removable component which is removed prior to use. This prevents self-discharge and can therefore be stored for long periods of time before being used. Secondary batteries are rechargeable and last according to their cycle life. Secondary batteries are further divided into Lithium ion (Li-ion), Nickel metal hydride (Ni-MH), lead acid, and Nickel cadmium (Ni-Cd). Since the development of portable electronics, the size of batteries has become smaller and smaller. Li-ion batteries are at the forefront of energy production in the latest technological developments such as smart phones, laptops and electric vehicles due to their high capacities, energy densities and improved rate capabilities. Lithium is relatively inexpensive and the lightest metal on the periodic table [14]. Lithium metal also has the highest standard reduction potential of – 3.04 V. This is higher than any of the other battery electrode

9

materials such as sodium (- 2.71 V), magnesium (-2.70 V) and aluminum (-1.66 V). This shows that Li-metal has the least tendency to be reduced in comparison to the above mentioned metals [8]. Figure 4 illustrates the relationship between volumetric and specific energy density in secondary batteries. It can be observed that Li-ion batteries have the highest energy density for amongst all secondary battery types.
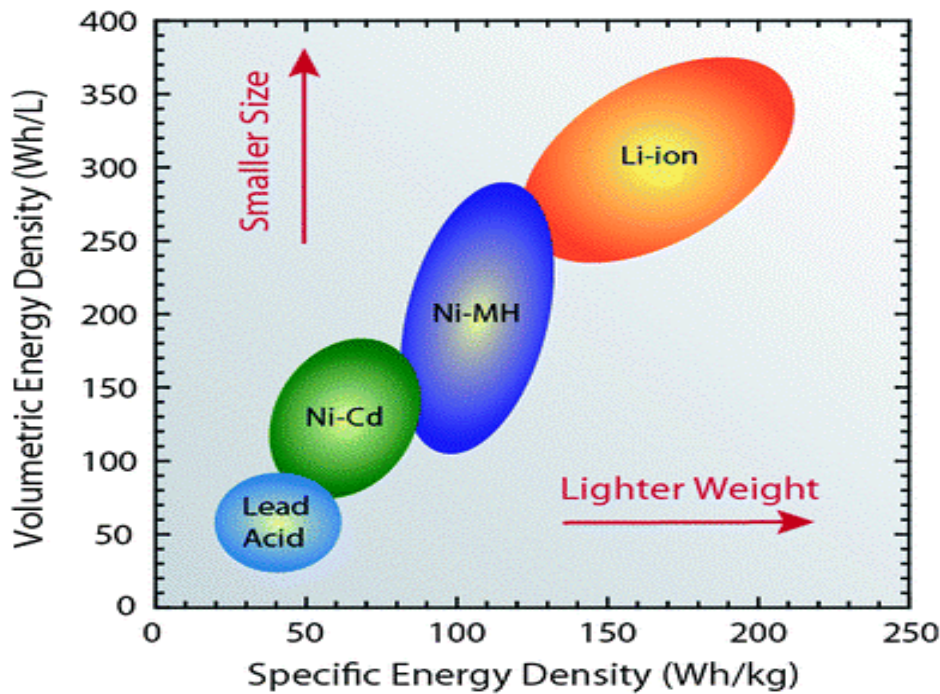
Figure 4: Volumetric vs specific energy density in secondary batteries [14]

Li-ion batteries have unique properties, but they also have a few concerning down sides. These include rapid capacity fading, decreased power and energy densities. Safety is also a concern as Li-ion materials are very reactive especially at elevated temperatures [15]. The cathode is the positive electrode and is also the biggest part of the Li-ion battery system and therefore is very important in providing the battery with energy. The most popular cathode materials for Li-ion batteries include; $LiCoO_2$, $LiMnO_2$, $LiFePO_4$, $LiNiO_2$ to name a few [15]. Lithium ion batteries have a global market value of 12 billion USD per annum and this has been estimated to increase to 25 billion USD by the end of 2017 [16]-[17].

10

1.6   Problem statement

In this study, I will be conducting extensive research on $LiMnO_2$ and its modification as a high-performance Li-ion battery cathode material. $LiMnO_2$ has attractive commercial properties. It is cheap, non-toxic and readily available in nature. Pristine $LiMnO_2$ however does have a few electrochemical issues when it comes to battery performance. The main problem is capacity fading due to Jahn-Teller distortion as a result of manganese dissolution into the electrolyte. In an effort to prevent the loss of capacity during cycling, I will be modifying the pristine $LiMnO_2$ cathode material with nano-AlF_3 and graphene. The coating of AlF_3 nanoparticles will minimize manganese dissolution and also improve cycle life. Graphene has immense electronic properties and will also aid in improving the electronic properties of the $[AlF_{3X}LiMn_2O_4$-Graphene] cathode material.

1.7   Objectives

- To develop a novel Li-ion cathode material which improves the structural and electrochemical stability of the pristine $LiMn_2O_4$ cathode material.
- To synthesize and characterize crystalline AlF_3 which serves as a protective layer to increase cyclability, rate capability and thermal stability of the pristine cathode material.
- To synthesize and characterize reduced graphene oxide (rGO) which improves the synergistic properties of pristine $LiMn_2O_4$.
- To determine the power density, energy density and the stability of the novel cathode material synthesized.

Chapter 2: Literature review

Chapter Overview

This chapter includes a review of various lithium ion cathode and electrochemical storage systems of lithium, their pros and cons as well as battery concepts. The anode in lithium ion batteries is also discussed in brief.

2.1 Developed battery technologies

Table 1: Comparison of Lead acid, NiCd and Li-ion battery properties [18]–[20]

	Lead acid	NiCd	Li-ion
Gravimetric energy density (Wh/kg)	30 - 50	45 - 80	110 - 160
Cycle life	200 - 300	1500	500 - 1000
Fast time charge (h)	8 - 16	1	2 - 4
Cell Voltage (V)	2	1.25	3.6
Operating temperature (°C)	-20 to 60	-40 to 60	-20 to 60
Maintenance (Month)	3 to 6	1 to 2	Not required
Commercial use since	1970	1950	1991

2.1.1 Lead acid batteries

The lead (Pb) acid battery is the oldest known secondary battery system invented by Gaston Plante′ in 1859[21]. It is mostly used in motor vehicles, energy storage and the telecommunications industry. The Pb acid battery is also used in hybrid electric vehicles [22]. Its nomenclature comes from the fact that lead is the active material in both the positive (PbO_2) and negative (Pb) electrode. The reaction which takes place in Pb acid battery follows below [23]:

$$\text{Cathode: } PbO_2 + H_2SO_4 + 2H^+ + 2e^- \rightarrow PbSO_4 + 2H_2O \qquad (17)$$

$$\text{Anode: } Pb + H_2SO_4 \rightarrow PbSO_4 + 2H^+ + 2e^- \qquad (18)$$

12

$$\text{Overall: Pb } + \text{ PbO}_2 + 2\text{H}_2\text{O}_4 \rightarrow \text{PbSO}_4 + \text{H}_2\text{O} \tag{19}$$
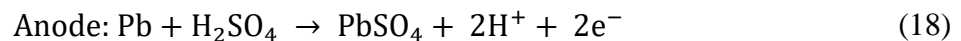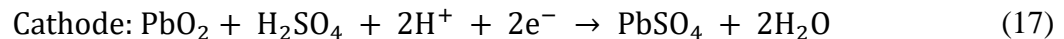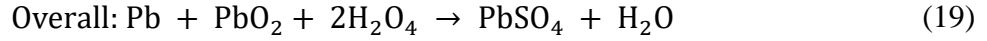
Pb acid batteries have been widely used and commercialized for a very long time. The success of the Pb acid battery is primarily due to its attractive properties such as non-toxicity, high cyclability, reliability, cost effectiveness, safety and easy design [24]. In Pb acid batteries, the nominal potential is $U^\circ = 2$ V. This is because the equilibrium voltages at the electrodes differ and depend on acid concentration. $U^\circ_{PbO_2} = 1.7$ V and $U^\circ_{Pb/PbSO_4} = 0.3$ V [24]. These voltage differences at the electrodes allows for secondary reactions to take place within the cell. These reactions are mainly hydrogen and oxygen evolution reactions which take place at the electrodes as can be observed in the reactions electrode below.

$$\text{Oxygen evolution at the cathode: } 2\text{H}_2 \rightarrow \text{O}_2 + 4\text{H}^+ + 4\text{e}^- \tag{20}$$

$$\text{Hydrogen evolution at the anode: } 4\text{H}^+ + 4\text{e}^- \rightarrow 2\text{H}_2 \tag{21}$$

$$\text{Water decomposition: } 2\text{H}_2\text{O} \rightarrow \text{O}_2 + 2\text{H}_2 \tag{22}$$
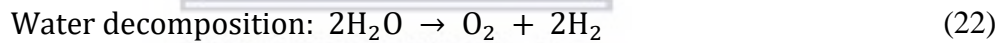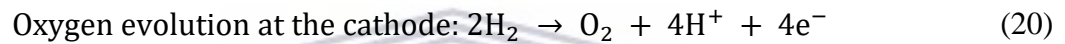
Pb acid batteries are continuously being studied and modified due to the hydrogen evolution aspect which decreases battery efficiency and contributes to safety concerns. Research also continues in order to maintain market competitiveness especially in emerging markets such as electric and hybrid electric motor industries. The actual energy density, 30-50 Wh/kg for the Pb acid battery is very low in comparison to its theoretical energy density, 162 Wh/kg [18]. Improvements in battery performance are usually done by incorporating lightweight carbon material or graphene derivatives in order to improve the electrical properties as well as to reduce the mass of the Pb acid battery [18].

2.1.2　Nickel-Cadmium batteries

Initial studies on the Ni-Cd battery were conducted in between 1899 and 1901 by Waldemar Jungner and Thomas Edison. The initial battery design had 2 issues namely; rapid capacity loss due to compaction and loss of porosity and swelling at the cathode which eventually led to capacity loss. In order to alleviate this factor, many improvements were performed on the Ni-Cd battery from the early 1900's up until World War II. This included the use of Cobalt, nickel strips, sintering of electrodes etc. Pocket and tubular Ni-Cd cells were tried but it was the innovation of the hermetically sealed Ni-Cd cell that proved to withstand high overcharge and thus providing long cycle life, compactness and increased energy density for a wide range of electronic applications. The active material at the cathode is NiOOH and Cd metal at the anode forming the Ni-Cd couple [25]. The electrode reaction can be observed below:

$$\text{Anode: } Cd + \ 2OH^- = Cd \ (OH)_2 + \ 2e^- \tag{23}$$

$$\text{Cathode: } 2NiOOH + \ 2H_2O \ + 2e^- \ = \ 2Ni(OH)_2 + 2OH^- \tag{24}$$

$$\text{Overall: } 2NiOOH \ + Cd + 2H_2O \ = 2Ni(OH)_2 + \ Cd(OH) \tag{25}$$
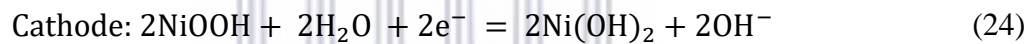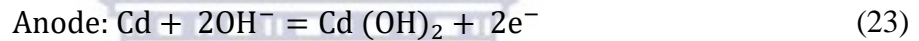
2.2　Lithium ion batteries

Lithium ion batteries are the most suitable power supplies for many portable electronic devices such as cellular phones, cameras and laptops. This is due to its high-energy density and rechargeable nature. Figure 5 illustrates a cross section of a standard Li-ion polymer cell used in variety of applications.

14
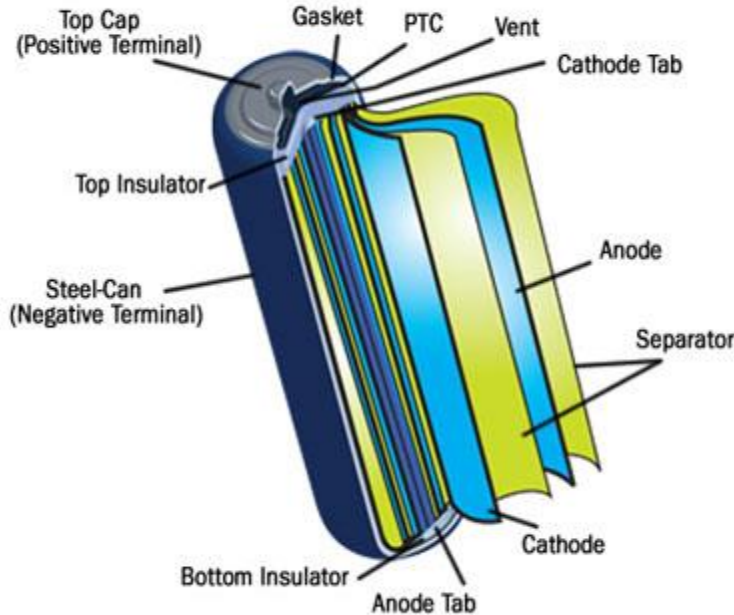
Figure 5: Cross-section of a polymer Li-ion cell [12]

Lithium ion batteries have no memory effect. This means that there is no need to discharge completely before recharging and it can handle many charge/discharge cycles. A Li-ion battery provides a 1.5 times greater weight energy density than the nickel metal hydride battery (Ni-MH). Li-ion batteries have a voltage of 3.7 V, which is three times more than the 1.2V nickel batteries of Ni-MH and NiCd. The Li-ion battery is also compact and light weight thus making it consumer friendly [20]. Sony commercialized the first Li-ion battery in 1991, and this chemical technology is today the most promising and fastest growing on the global market. Li-ion batteries are also being incorporated in military devices, electric vehicles, hybrid electric vehicles and aerospace engineering [19]. There is therefore a huge need for more efficient ways of storing energy so that it can be readily available when needed to power some of these technological devices.

The power density of the Li-ion battery is relatively low because of large polarization at high charge-discharge rates in electronic devices. This polarization is caused by slow lithium diffusion in the active material and increased resistance of the electrolyte when the charging-discharging rate is increased. To overcome these problems, it is important to design and fabricate nanostructured electrode materials that provide high surface area and short diffusion paths for ionic transport and electronic conduction. Nanomaterials offer extraordinary mechanical, electrical and

15

optical properties to Li-ion battery materials, which can improve its energy and power capacity [26].

2.2.1 Operating procedure of Li-ion batteries

In the standard Li-ion battery, lithium ions (Li^+) flow from the cathode to the anode when charging and from the anode to the cathode during discharge as illustrated in Figure 6 below. When the Li-ion cell discharges, the oxidation half reaction at the cathode is: Error! Reference source not found.
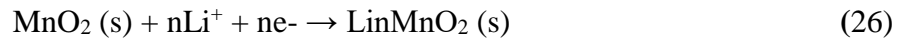
$$MnO_2 \text{ (s)} + nLi^+ + ne\text{-} \rightarrow Li_nMnO_2 \text{ (s)} \tag{26}$$

The cathode is generally made from lithium metal oxides such as lithium cobalt oxide and lithium manganese oxides. The anode is made from graphite or silicon-based alloys of lithium metal. The cathode material of interest to me is $LiMn_2O_4$. This is due to low toxicity compared to other metal oxide cathode materials, low cost and readily available Mn [28]. When the Li-ion cell discharges, the oxidation half reaction at the anode is:

$$LiC_6 \rightarrow C_6 + Li^+ + 1e^- \tag{27}$$
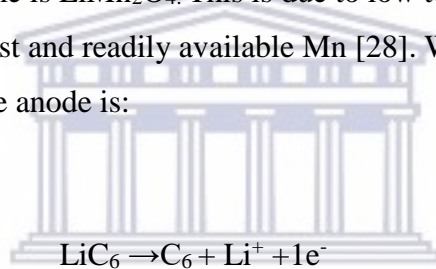
The cathode of a lithium ion battery must undergo a reduction reaction which consumes the electrons and lithium ions produced at the anode. Manganese oxide is an inorganic solvent which can serve this role [27]. The reduction half reaction is:
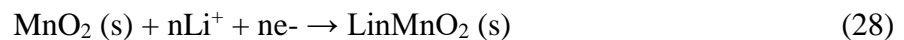
$$MnO_2 \text{ (s)} + nLi^+ + ne\text{-} \rightarrow Li_nMnO_2 \text{ (s)} \tag{28}$$

The cathode is generally made from lithium metal oxides such as lithium cobalt oxide and lithium manganese oxides. The anode is made from graphite or silicon-based alloys of lithium metal. The cathode material of interest to me is $LiMn_2O_4$. This is due to low toxicity compared to other metal oxide cathode materials, low cost and readily available Mn.

16
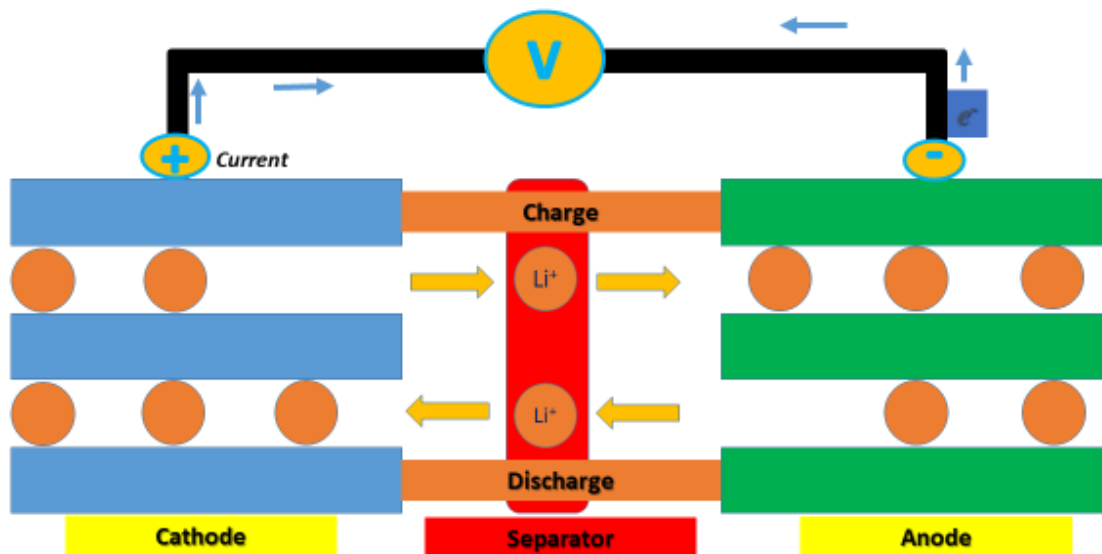
Figure 6: Illustrating operating procedure of Li-ion battery

2.2.2 Anodes in Lithium ion batteries

The anode is the negative electrode in a lithium ion cell. Oxidative processes take place here and electrons are released as a result. Lithium metal has been identified as the best anode material in lithium ion cells due to the fact that it is able to conduct both lithium ions as well as electrons. Lithium metal is also known as the most electronegative metal (-3.06 V) and high surface to volume ratio which gives rise to high capacities. Lithium metal however encompasses dendritic growth as a result of many charge/discharge cycles. It is also very volatile (explosive) [29]

2.2.2.1 Carbon based anodes

Today, the most commercially viable anode material for lithium ion batteries is graphite (372 mAh.g^{-1}) [30]. Graphite is ionic and electron conductive. It also allows for reversible lithium ion insertion and extraction during cycling, hence preventing dendritic formation on the electrode surface. This redox process can be observed in equation (29) below. The power and energy density standard requirements of LiBs are changing on a regular basis. It is for this reason that carbon based anodes need to be modified in order to meet the demand for higher capacities [30]. Apart from the low capacity of graphite, it also has a high electrical and thermal resistance

17

$$6C \ + \ xLi + \ + \ xe^- \ \leftrightarrow \ Li_xC_6 \qquad (29)$$

2.2.2.2 Graphene-metal oxide Composites

In order to improve anode storage capacity requirements in LIBSs, scientists have employed a range of 1D and 2D carbon-based nanomaterials to be used as graphite substitutes. These include nanotubes and graphene. Thin layer nanostructured materials are used because they are lightweight, possess high surface area and have good mechanical properties. Zhang *et al.*, 2017 used CoO/Co_3O_4/graphene as an anode material and found that the nanocomposite anode material had a high capacity of 825 mAh.g^1. Other graphene based anode materials which also yield high capacities include, Au,Si-graphene (2210-1520 mAh.g^{-1}), SiO_2-gpahene (2700- 1300 mAh.g^{-1}), Fe_3O_4 (1750-1130 mAh.g^{-1}), where the value before the dash (-) is the capacity at the 1st cycle and the number after the (-) is the capacity at the last cycle [31]. It is to be noted that the above-mentioned metal oxides have poor cyclic performance. This is caused as due to anode upon Li^+ insertion/extraction volume expansion. The inclusion of graphene to the metal oxide and forming an anode composite would alleviate this problem as discussed by Zhou *et al.*, 2013 where an advancement in electrochemical and structural performance was made [32].

2.2.3 Cathode materials in Lithium Ion batteries

The cathode is the largest part of a Li-ion battery and the second most expensive component [33]. There are solid, liquid and gas cathodes as well as intercalation cathodes in Li-ion batteries. At the cathode, electrons and lithium ions produced at the anode are consumed. A typical example of a solid cathode is Iron disulphide. Its half-reaction is:

$$FeS_2(s) + 4Li^+ + 4e^- \rightarrow Fe(s) + 2Li_2S(s) \qquad (30)$$
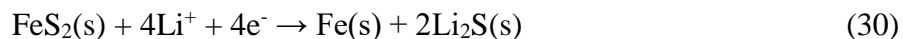
Thionyl chloride is a common example of an inorganic liquid that can serve as a cathode material. Its half-reaction is:

18

$$2SOCl_2(l) + 4Li^+ + 4e^- \rightarrow S + SO_2 + 4LiCl(s) \qquad (31)$$
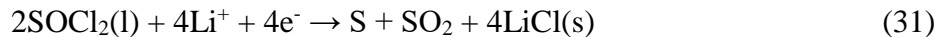
An example of a gaseous cathode reactant material which is also used in Li-ion batteries is sulfur dioxide gas. The sulfur dioxide is dissolved in the electrolyte solution and a current collector is placed in contact with the sulfur dioxide liquid cathode. The cell reaction is:

$$2Li(s) + 2SO_2 \rightarrow Li_2S_2O_4 \qquad (32)$$

2.2.3.1 Intercalation Cathodes

There are three main intercalation cathode materials which are used in Li-ion batteries. These materials include; $LiCoO_2$, $LiNiO_2$ and $LiMnO_2$ [26]. $LiCoO_2$ is found to be the most popular due to the fact that it's easy to synthesize using both the solid state and chemical approaches. Li_xCoO_2 exhibits excellent cyclability at room temperature for $1> x > 0.5$. The specific capacity of $LiCoO_2$ is limited to the range of 137 to 140 $mAh.g^{-1}$ [26]. Even though the theoretical capacity of $LiCoO_2$ is 273 mAh/g^{-1}. The downfall of the $LiCoO_2$ cathode, materials is that it's very costly and found to be highly toxic. The reversible capacity of Li_xNiO_2 is higher than that of Li_xCoO_2 since the amount of lithium that can be intercalated during redox cycles is around 0.55 compared to 0.5 for $LiCoO_2$, this allows the specific capacity to be greater than 150 $mAh.g^{-1}$ with appropriate cyclability. The preparation of $LiNiO_2$ is much more complex than that of $LiCoO_2$, and this is due to the additional nickel ions on the lithium sites. The Li-Ni-O system can be represented by $Li_{1-y}Ni_{1+y}O_2$. This special structure makes it very difficult to synthesize the stoichiometric oxide with all the lithium sites completely filled by lithium. This leaves us with the $LiMnO_2$ cathode material, where LiO_2 serves as the host material onto which the manganese ions will intercalate [26]. When in comparison to $LiCoO_2$ and $LiNiO_2$, $LiMn_2O_4$ is far less toxic and its materials are easier to source and put together. $LiMnO_2$ permits the intercalation of Li-ions in the range $0 < x < 2$ [26]. The intercalation of Li-ions decreases the average valence of manganese ions and leads to a pronounced Jahn-Teller effect in which the cubic spinel crystal becomes distorted tetragonal with

19

c/a = 1.16. This is known as the axial ratio for a hexagonal close packed structure. The ideal axial ratio is c/a = 1.66. The lower c/a ratio causes a low capacity restricted to 120-125 mAhg^{-1} as well as significant capacity degradation at high temperatures [26]. Capacity fading is due to phase transition from cubic to tetragonal upon 3-4 V prolonged cycling, micro-crack formation on the surface of the cathode material after electrochemical cycling, formation of a surface dead layer and formation of oxygen vacancies due to dissolution of manganese in the electrolyte at elevated temperatures [20]. The 3D spinel channel (8a-16c-8a) is favourable for the intercalation/ deintercalation of Li$^+$ ions [34]

2.2.3.2   Nanotechnology in Lithium ion cathodes

There are many nanotechnology methods that can be implemented in improving the capacity efficiency and surface instability of $LiMn_2O_4$ cathode material. These include surface coating, which modifies the surface of the material by coating it with nanoparticles of various elements, laser annealing which is used for the crystallization sample material into thin electrodes [35] and doping which improves the bulk properties of the cathode material. In the $LiMn_2O_4$ cathode, coating and doping serves as a means in which researchers try to inhibit capacity fading and improve electrochemical performance in modified $LiMn_2O_4$ cathode systems, it also weakens the Jahn-Teller effect caused by Mn^{3+} ions at the octahedral sites and improves the stability of the structure. This can be illustrated in the following redox reaction: $Li^{4+} + 1e^- \rightarrow Li^{3+}$ [36]. The $LiMn_2O_4$ cathode can be doped with various metals and non-metals, these include; B, F, S, Br, Mg, Al, Ti, Cr, Fe, etc [20]. Pristine $LiMn_2O_4$ can be coated with various materials which are chemically stable and are ion conducting. This is true for AlF_3 which has a high ionic conductivity, is chemically and electrically stable due to the strong [Al-F] bonds which are able to decrease oxygen activity on the electrode surface during cycling [37] .

20

2.2.3.3 The Spinel framework
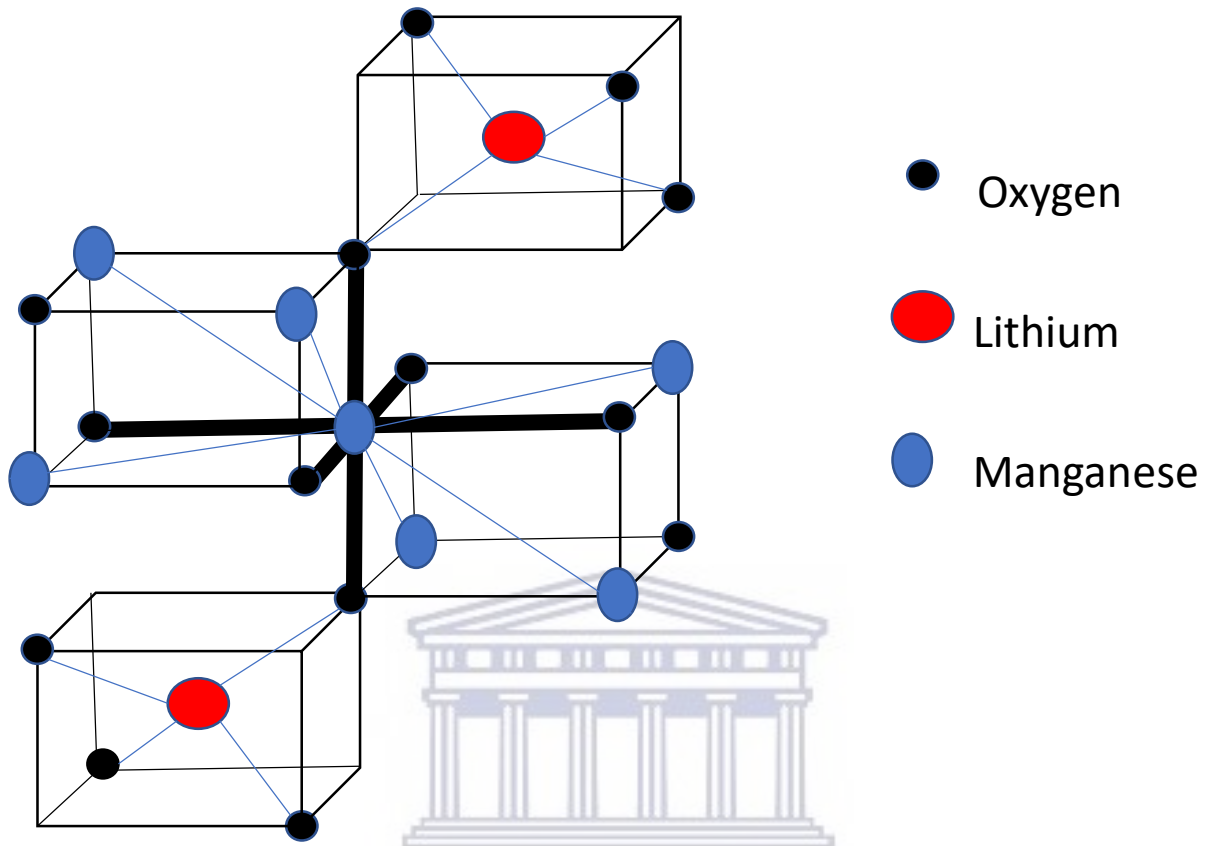
Figure 7: Unit cell segment showing the coordination of ions in LMO lattice [28]

LMO forms a spinel structure in which manganese is located in the octahedral (16d) sites, lithium occupies the tetrahedral (8a) sites and oxygen occupies the 32e sites in a unit cell. Li-ion intercalation/ deintercalation occurs in a 3D channeled network [28]. This can be observed in the Figure 7 above. Where Mn-O bonds and Mn-chains can be seen. The spinel is very attractive for battery technology as it allows for good lithium ion transport from the tetrahedral (8a) sites within the spinel. The LMO spinel is non-toxic, readily available and very cost effective. LMO has a cubic spinel structure with Fd3m space group symmetry   Orthosilicates also form part of the spinel family, Li_2MnSiO_4; [M] = Mn, Fe, Co, Ni.

2.2.3.4 The layered oxides

Lithium containing layered oxides can be expressed as $Li[M]O_2$ (M = Co, Ni). $LiCoO_2$ is currently the world's leading battery cathode material with an energy density of 150 $WhKg^{-1}$ [38]. Layered oxide materials used as cathodes have a few downsides, these include oxygen evolution at high charging potentials, high toxicity, they are expensive due to the high cost of Co and have safety concerns with regard to practical applications in hybrid electric vehicles and electric vehicles. Layered oxides, even though they are widely commercialized, do not have a bright future in next generation battery technologies [38]. Figure 8: Layered structure showing lithium ions between transition metal oxide sheets [39]. Figure 8 below illustrates the general structure of the layered cathode [39].
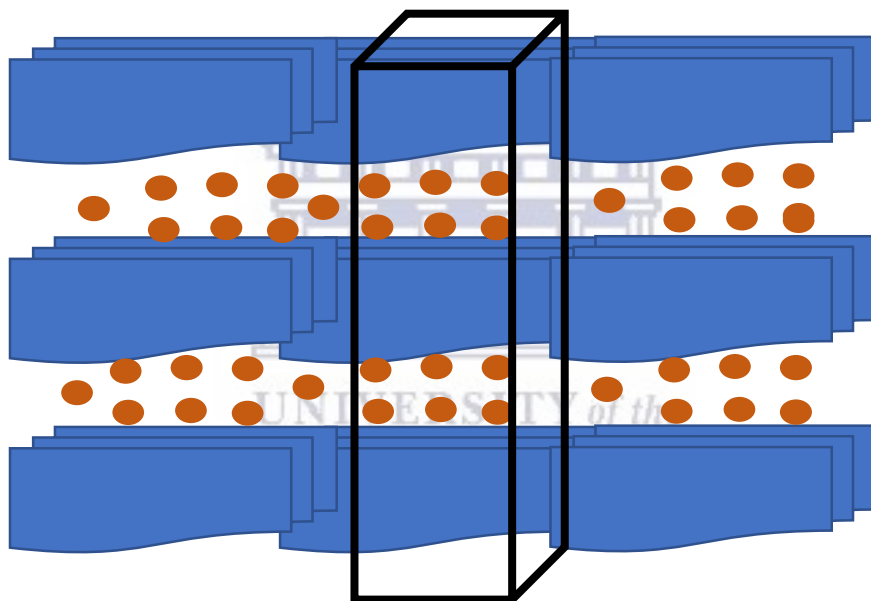
Figure 8: Layered structure showing lithium ions between transition metal oxide sheets [39]

2.2.3.5 The Olivine

The most popular cathode material with an olivine structure is $LiFePO_4$ (LFP). LFP is cheap and readily available in nature. LFP has been a cathode material of interest to be employed in electric vehicles and hybrid electric vehicles [40]. In LFP, Phosphorous occupies the tetrahedral sites, iron occupies the octahedral sites and the Li-ions form 1D chains in the [010] direction. The 1D chains allow for ion exchange to take place. Although LFP has good reversibility and cyclability [41]. It has been reported that LFP has a low ionic conductivity in the range of (10^{-9} $S.cm^{-1}$) and low

electronic conductivity [42]. Various modification methods have been tried in order to improve the conductivities of LFP. These include; grain shade and size alterations as well as the addition of electronic conductive additives such as graphene [43]. Olivine structured materials (Fe_3O_4 and $Sn-Fe_2O_3$-C have also been used as electrochemical stable anodes where capacities in the range of 900 mA.g^{-1} and high current densities were obtained [44].

2.3   Electrolytes

The electrolyte in lithium ion batteries serves as a transport medium through which lithium ions can travel between the electrodes during the charge/discharge process [39]. The electrolyte is very important as it is a major determining factor in the specific capacity, energy density as well as the lifespan of the battery [38]. Electrolytes in LIB's must meet a specific standard, this include:

- Chemical and thermal stability at ambient/ operating temperatures
- Li-ion conductivity> 10^{-4} S cm^{-1}
- electronic conductivity < 10^{-10} S cm^{-1}
- Consistency of electrode/electrolyte interface
- User and environmentally friendly

Electrolytes can also transfer electrons to the electrode material or *vice versa*, depending on the electron potential range of the electrolyte used [45].

2.4   Thermal instability of LiMn$_2$O$_4$

Pristine LiMn$_2$O$_4$ has been proven to become unstable at elevated temperatures in excess of 55 ℃. At increased temperatures, the LMO cathode material becomes unstable and severe capacity fading occurs. The capacity loss hinders applications for Li-ion batteries as well as its operating potential range of approximately 4 V [34]. This is due to manganese dissolution into the electrolyte according to the Mn disproportion reaction as seen below [46]:

$$2Mn^{3+}(s) \rightarrow Mn^{2+}(aq) + Mn^{4+}(s) \tag{33}$$
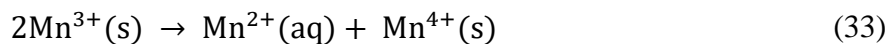
This Mn dissolution also causes structural instability, as the cubic spinel would distort and become orthorhombic and shape due to Jahn-Teller effects [47]. As a result, less lithium ions will be

23

allowed to intercalate/deintercalate between cathode and anode during charge/discharge processes and therefore lower cathode capacities will be reported. Various strategies have been employed in order to mitigate the capacity fading challenges which are caused by thermal instability and long cycling periods. These include, surface modification through coating procedures, cationic and anionic doping with metals and non-metals alike, particle shape and size modification as well as electrolyte optimization techniques which allow improved migration of Li-ions through the electrolyte [47]. Pristine $LiMn_2O_4$ was first coated with 2% SrF_2 by J.G. Li *et al.,2012* and proved that a 97% capacity retention is observed after 20 cycles at 55 ℃ compared to that of the unmodified LMO which retained 79% of its cycling capacity at the same temperature[48]. Other coating methods such as MgF_2 and TiO_2 also showed improved capacities of LMO at elevated temperatures, reduced electrolyte oxidation, as well as enhanced Li^+ diffusion were reported [34]. Zhange et al., found that TiO_2-coating of LMO substantially reduces Mn dissolution into the $LiPF_3$ electrolyte and as a result a smaller capacity loss was reported after 250 cycles [34]. In our effort to reduce capacity fading through Mn dissolution, AlF_3-coating of LMO will be employed before placing the active material onto a graphene template so as to obtain optimum structural and electrochemical stability of the modified LMO.

2.5   Graphene in Lithium ion batteries

Single layer graphene was first isolated in 2004 by Novoselov *et al.*, in 2004 using the simple yet effective mechanical exfoliation or scotch tape method [49]. Graphene has been found to possess various superior qualities to most materials and can be seen as a technology of the future. These qualities include; excellent electrical conductivity due to charge carries which have relativistic particle properties [50], extremely high surface area (2600 $m^2.g^{-1}$) and good elasticity. Graphene has a thickness of atomic proportions. This means that it is a 2D porous material which exposes every C-atom to the surface, which may provide a matrix on which to grow electrode materials such as $LiMn_2O_4$ with negligible electrical resistance due to the fact that it's one atom thick nature [51]. This porous carbon network could provide multitudes of space for electrode expansion upon Li-ion insertion and serve as a means to decrease capacity loss after longer cycling periods and excessive heat. Graphene is an aromatic material which is in the sp^2 hybridized state. The covalent bonds of 0.142 nm in length between carbon atoms allow for a polymer network with robust

24

strength like none other [52]. The honeycomb lattice gives a strength to weight ratio which is higher than the strongest of metal alloys [53]. Its robust nature does not prevent elasticity. Graphene is therefore flexible and forms various allotropes such as nanotubes, nanowires, fullerenes etc. which can be employed in various electronic and biomedical applications [54].

The application of graphene in LiBs have been described before. *Lui et al.,2014* found that TiO_2/rGO as and anode material using a surfactant-templating assembly coating method significantly improves the specific capacity due to increased surface area in the range of 137 m^2.g^{-1} [55]. *Wang et al.,2014* used graphene as a template catalyst onto which $MnCoO_2$ was grown onto through covalent bonding. The honeycomb lattice of graphene allows for carbon-oxygen-metal bonding [C-O-M]. it was found that the graphene modified transition metal cathode material displayed improved cycle life and no coating degradation after 10 cycles [56]. This due to the electronic and structural stability that graphene holds [56]. The carbon structure in graphene forms a unique honeycomb crystal lattice which allows it to be an excellent electron charge transfer material. In this study, graphene is to be synthesized using the modified Hummers method. The graphene sheets will serve as a template onto which it becomes functionalized with $AlF_3LiMn_2O_4$.

2.6   Aluminium trifluoride coating

Surface coating has previously been used to stabilize $LiMn_2O$/electrolyte interface. This structural stabilization method makes use of an artificial material layer which served to protect the active layer. Various coating alternatives have been used before. These include; Al_2O_3, ZrO_2, MgO as well as metal phosphates such as $AlPO_4$ [57]. Fang *et al.,*2013 made use of graphene-oxide as a coating material for $LiMn_2O_4$ as a means to prevent Mn dissolution into the spinel through the Mn disproportionation reaction which is seen in equation (33)above [58].

The employment of aluminium trifluoride (AlF_3) coating serves to improve the structural and electrochemical properties of the pristine $LiMn_2O_4$ cathode material [59]. AlF_3 has high ionic conductivity, chemical and electrochemical stability. Al-F bonds are strong and stable and reduces oxygen activity on the surface of the cathode during cycling. AlF_3 generally has high surface areas in the range of 10-50 m^2/g due to its high lattice energy [60]. A thin layered AlF_3 coating will improve electrochemical properties such as cyclability, rate capability and thermal stability. Wu

*et al.,*2015 observed no deviations in the bulk structure of the AlF_3 coated material as compared to the pristine $Li[Ni_{1/3}Co_{1/3}Mn_{1/3}]O_2$ cathode. This simply means that there are no intrinsic structural defects after coating. This concept is also confirmed by Liu *et al.,*2008 where the AlF_3 coating did not affect the spinel structure of $LiMn_2O_4$ [61].

Chapter 3: Materials and Methods

Chapter Overview

Chapter 3 gives a basic outline of the methodology employed in obtaining the pristine cathode material (LiM_2O_4) as well as the novel [$AlF_3LiMn_2O_4$-rGO] 70% wt. $LiMn_2O_4$, 20% wt. AlF_3 and 10% wt. rGO cathode material studied and the characterization thereof.

3.1   Reagents and Materials

The chemical reagents used in this study are as follows: Manganese (II) acetate (99 %), Lithium Hydroxide (99 %), Sulphuric Acid (99 %), Graphite powder, Potassium permanganate, Sodium borohydride, aluminium fluoride trihydride. These reagents were purchased from Sigma-Aldrich and N-methylpyrrolidinone (NMP) (99 %), was purchased from Alfa Aesar. Analytical grade argon (Afrox, South Africa) was used to degas the system. Laboratory grade deionised water was used for all reactions.

3.2   Characterization of structural properties

The following techniques and instrumentation are mandatory for the characterisation and fundamental understanding of the synthesized material.

3.2.1   X-ray diffraction (XRD)

XRD is a technique used to determine the crystal structure of a material. X-rays are incorporated to penetrate through the material of interest and gives the respective diffraction pattern which is the atomic and molecular pattern specific for that material. XRD is used in material analysis in order to identify the crystalline phase of the material synthesised. XRD allows for the determination of lattice parameters using the least squares method [62]. XRD also determines space group structure and symmetry. XRD plays a pivotal role in characterizing the $LiMn_2O_4$ crystal structure. We are thus able to determine whether the spinel was formed as well as to which space group symmetry was obtained from the sol-gel synthetic route used. XRD measurements

27

were carried out with the BRUKER AXS (Germany), D8 advanced diffractometer, using Cu-Kα radiation ($υKα$ =.5406 Å). The diffraction patterns were taken at room temperature in the range of $5 < 2Θ > 90°$ using step scans.

3.2.2 Surface morphology by SEM and HRTEM

Electron microscopy is an essential set of characterization techniques which comprise of an electron beam which travels through a vacuum before interacting with the nanomaterial. HRTEM is focussed on the surface of the material and HRTEM targets the intrinsic properties of the material such as structure and crystallinity.

3.2.3 High resolution scanning electron microscopy (HRSEM)

HRSEM is based on a scanning principle whereby an electron beam produced by an electron gun travels through a vacuum and scans over a selected area on the surface of the material. It then forms a three-dimensional electronic image of the morphology and topography of the material. This occurs due to secondary electrons which are detected due to their low energies. HRSEM also gives details about the elemental composition of the material of interest. HRSEM showed the growth of the $LiMn_2O_4$ spinel as well as the modified novel cathode composite material. The ZEISS ULTRA scanning electron microscope was used for HRSEM analysis. A spatula tip amount of sample was dispersed on a carbon supported by alumina and sputter coated for 5 min with a gold-palladium alloy to make the samples conductive.

3.2.4 High resolution transmission electron microscopy (HRTEM)

HRTEM is an electron imaging technique which allows us to analyse the intrinsic properties of a material of interest. This includes material crystalline structure and phase. The high intensity beam passes through the material and is able to determine its properties. The properties of Most nanomaterials are studied using HRTEM imaging. These include, quantum dots, nanotubes and nanowires. Lattice parameters of nanomaterials are imaged and can be quantified adequately. The elemental composition of the material of interest is also determined the HRTEM analysis. In this

study, HRTEM analysis confirmed crystallinity and also determined how the lattice fringes structurally changed after modification of the pristine $LiMn_2O_4$ cathode material.

3.2.5   Fourier transform infrared spectroscopy (FTIR)

FTIR is used to determine how atoms are bonded together, surface characterization, how their pi arrangement is assembled (single, double and triple bonds), as well as the determination of the functional groups present in a particular molecule [60]. In FTIR, molecular vibrations are triggered by irradiation with infrared light. Upon excitation with infrared light, certain bonds vibrate faster, this is detected and can be interpreted in an infrared spectrum. This interpretation requires pattern recognition against the IR table. IR spectroscopy gives information about the bond length as well. It tells us whether a particular bond is stretched, compressed or at equilibrium. Covalent bonds vibrate at different vibrational modes, these include stretching, rocking and scissoring. Figure 9 below illustrates the respective vibrational modes in FTIR spectroscopy. In this work, the vibrational mode determinations of the pristine $LiMn_2O_4$ as well as the novel cathode material was conducted. KBr was used as the blank for this technique and was mixed with the samples (pristine and modified Li-ion materials) of interest to form penny sized pellets.
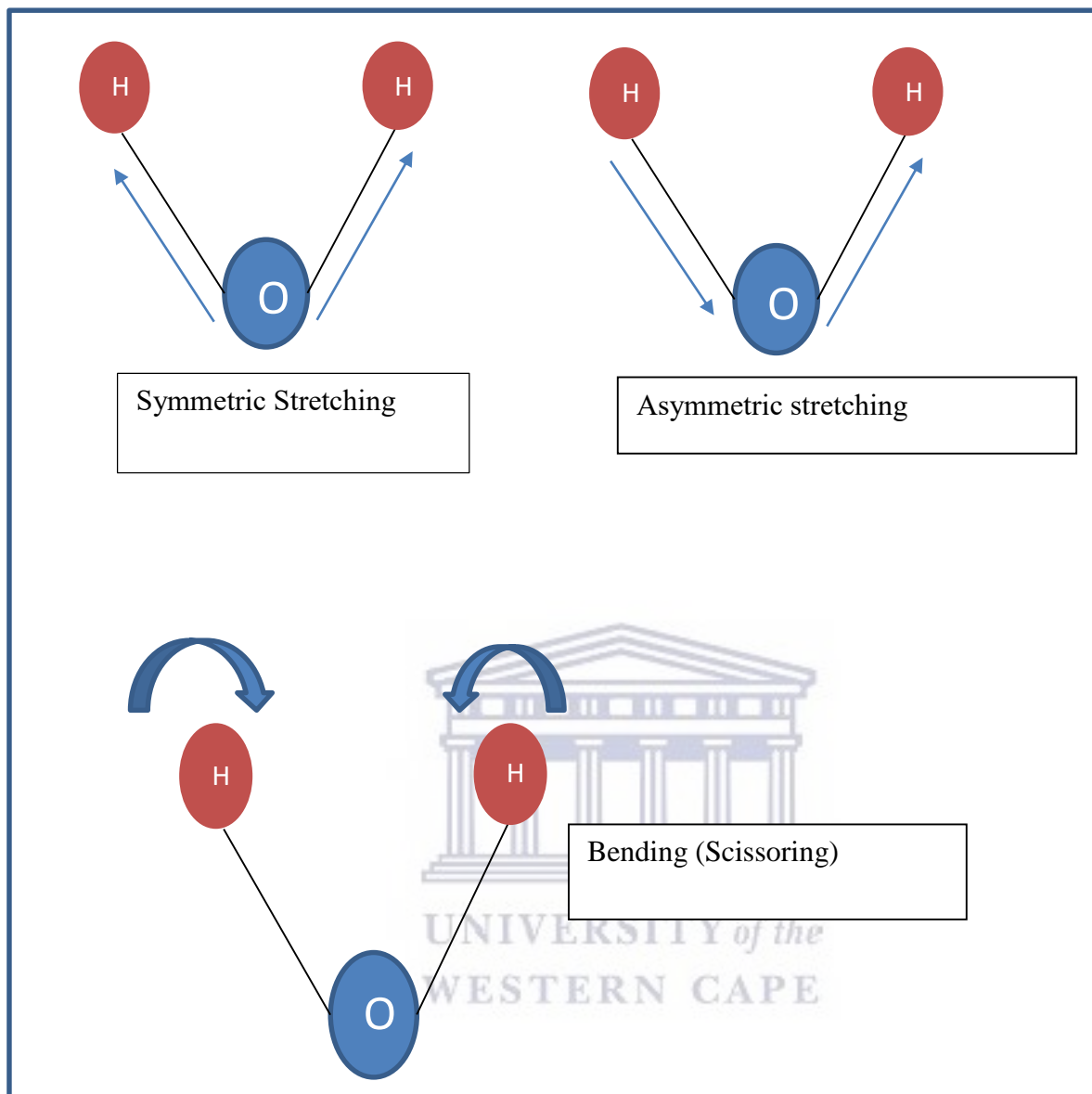
Figure 9: Vibrational modes in FTIR spectroscopy

3.2.6   Raman spectroscopy

Raman spectroscopy provides a fast and non-destructive analysis in the identification of graphene layers in determining how many layers are present in the graphene material. This technique was first invented by Indian physicist CV Raman in 1928. Raman spectroscopy relies on the scattering of light by a material where light is scattered inelastically as opposed to the more prominent

Raleigh scattering. Wavelength shifts are caused due to this inelastic scattering which can be used to extract information about the material being analysed. There is a net energy gain/loss in photons during the inelastic scattering process and thus a change in wavelength occurs. Raman spectroscopy can be further understood through stokes/anti-stokes scattering. Stokes scattering occurs when the molecule is promoted form ground state to virtual then drops back to a higher energy vibrational state [63]. The scattered photon will have less energy than the incident photon and therefore a longer wavelength. If the scattered photon has more energy and shorter wavelength, it's called anti-stokes scattering. Figure 10 describes the difference between Raleigh and raman scattering. The shift due to the raman effect is determined by the spacing between the vibrational states and the ground states. The stokes and anti-stokes scattered spectrum will be shifted an equal distance on opposite sides of the Raleigh scattered light [63].
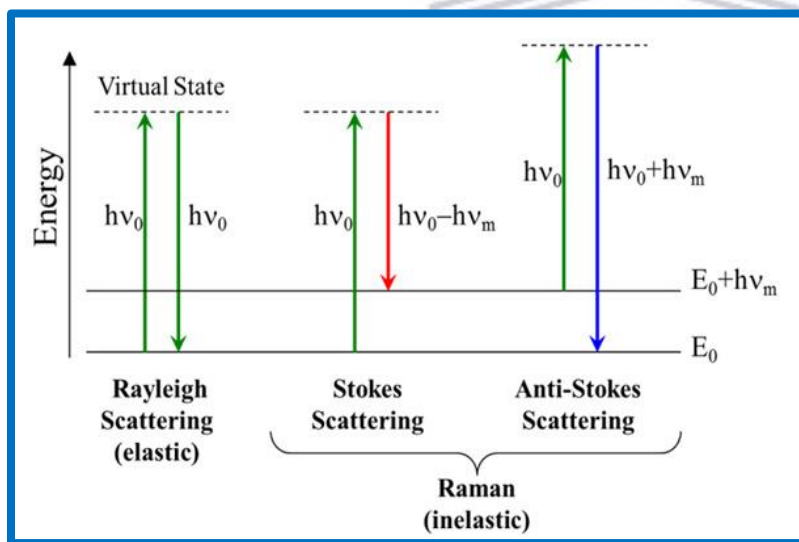

Figure 10: Jablonski Diagram Representing Quantum Energy Transitions for Rayleigh and Raman Scattering [63]

In this project Raman spectroscopy was used to study the vibrational information about octahedral MnO_6 and tetrahedral LiO_4 and how the vibrational structure of the pristine $LiMn_2O_4$ cathode material changed after AlF_3 coating and the addition of rGO support. Raman results were obtained using a Dilor XY Raman spectrometer with a Coherent Innova Argon laser with a 514.5 nm laser excitation.

3.3   Electrochemical techniques

In this work, all electrochemical studies were done on a CH Instruments electrochemical workstation, 600 E potentiostat (USA). The 3-electrode system was compiled of a glassy carbon (GCE) Working electrode, a Ag/AgCl reference electrode and a platinum wire as the counter electrode. The electrolyte solution used was $LiNO_3$. All experiments were carried at room temperature in an argon atmosphere. The setup of the 3 electrode setup can be observed in Figure 11 below:
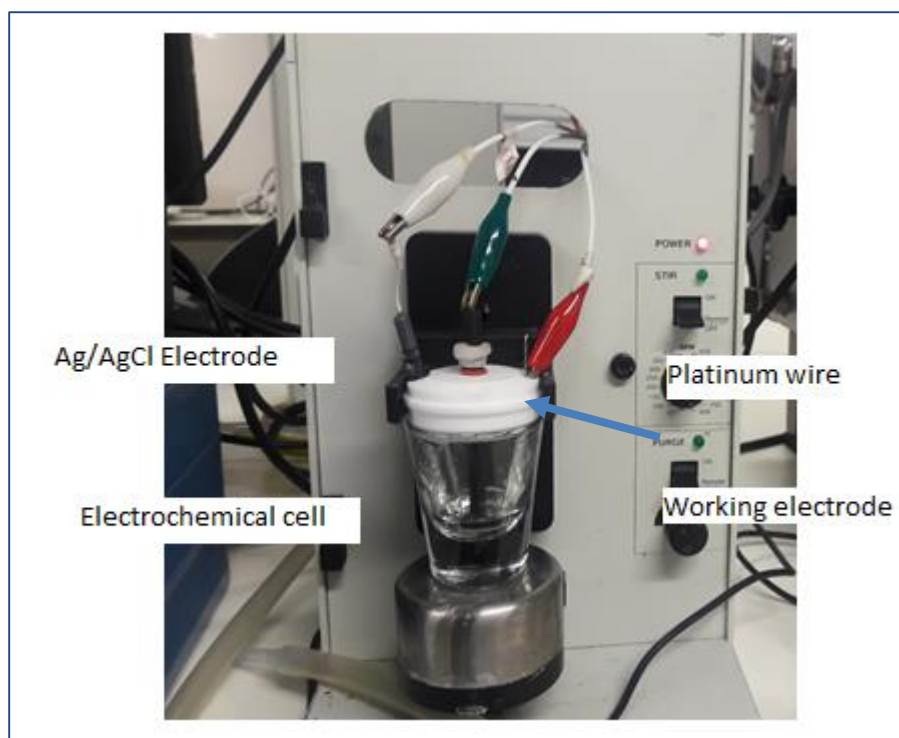

Figure 11: A typical 3 electrode system setup

3.3.1   Cyclic voltammetry (CV)

Cyclic voltammetry is a common electrochemical technique for obtaining qualitative and quantitative information regarding electrochemical reactions taking place on the surface of the working electrode. In a typical electro-analytical study, sweeps are carried out across a potential window which is preferable for the material being analysed. The current runs from the initial potential (E_i) towards the upper limit potential (E_f) and reversed back to the initial potential. This is known as a sweep. Cyclic voltammograms are run at varying scan rates (v). The peak current

http://etd.uwc.ac.za

density (Ip) is proportional to the scan rate used and depending on peak position, the reaction can be classified as either, reversible, non-reversible and quasi-reversible. The cyclic voltammogram in Figure 12 below shows an example of a reversible reduction/oxidation (REDOX) reaction.
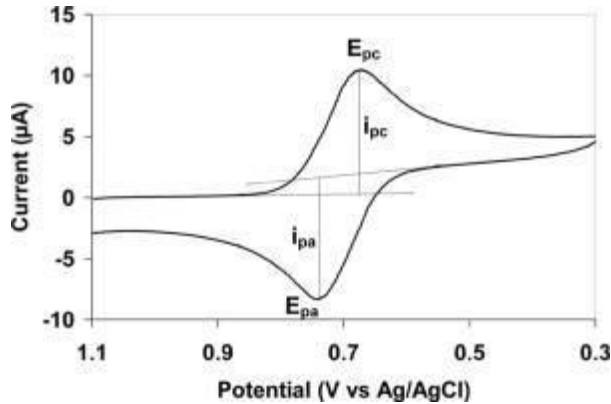

Figure 12: A representative example of a reversible electrode reaction process

The peak potentials in CV can be used to determine a range of parameters including concentration, formal potential, current density, capacity, electrode kinetics etc [64].

These parameters and more can be obtained by manipulations of the Randels Sevcik equation below [64]:

$$Ip = 2.69 \times 10^5 n^{3/2} A D^{1/2} C v^{1/2} \tag{34}$$

Where, Ip is the peak current (A), n is the number of electrons, A is the electrode area (cm^2), D is the diffusion coefficient ($cm^2 s^{-1}$), C is the concentration (mol. cm^{-3}) and v is the scan rate (mV.s). For an irreversible process, the following representation of the Randels Sevcik equation is observed.

$$Ip = 2.69 \times 10^5 \alpha^{1/2} n^{3/2} A D^{1/2} C v^{1/2} \tag{35}$$

Where Ip is the peak current, α is the transfer coefficient, n is the number of electrons, A is the electrode area (cm^2), D is the diffusion coefficient ($cm^2.s^{-1}$), C is the concentration (mol. cm^{-3}), and v is the scan rate (mV.s^{-1}). The charge capacity (Q) of the cathode material is given by:

$$Q = \frac{Area (AV)}{Scan\ rate\ (V.s^{-1})} \tag{36}$$

33

And can further be manipulated to give the specific capacity in the following equation:

$$\text{Specific capacity} = \frac{Q\ (Ah)}{\text{Active mass (g)}} \qquad (37)$$

1 M LiNO$_3$ solution was used as the electrolyte solution.

3.3.2 Square wave voltammetry (SWV)

Square wave voltammetry is an electrochemical characterization technique similar to CV in that it determines current density over a certain potential range. This technique however, only determines oxidation and reduction reactions on their own in comparison to the complete REDOX reaction seen in CV. It is therefore more sensitive than CV and exact oxidation/ reduction couples can be obtained. SWV was employed in this study in order to confirm the presence of redox couples indicating extraction of lithium ions from the tetrahedral sites in the spinel.

3.3.3 Electrochemical impedance spectroscopy (EIS)

Electrochemical impedance spectroscopy is required in order to determine the transport, electronic and ionic conductivity of materials [64]. Oliver Heaviside described EIS as a technique used to study electrode processes and reactions taking place on the surface of the electrode [65]. EIS employs an alternating current (AC) as a measure of the resistance observed when charge is passed across the surface of a material of interest, charge transfer resistance (R$_{ct}$). Impedance studies are analysed using the nyquist plot which is the Real impedance (Z$_{re}$) vs imaginary impedance (Z$_{im}$) or bode plot which is the modulus of impedance log/Z/ and the phase angle ψ between AC potential and AC current as a function of the frequency logω [66]. Examples of these can be observed in the figures below. EIS is of particular importance to this study, as it is used to determine the electron transfer kinetics as well as the diffusion properties of lithium ions. Theoretically LiMn$_2$O$_4$ has a higher R$_{ct}$ which causes longer charge transfer frequencies. The reduction of R$_{ct}$ will allow for faster charge transfer and electron transport within the cathode [15].
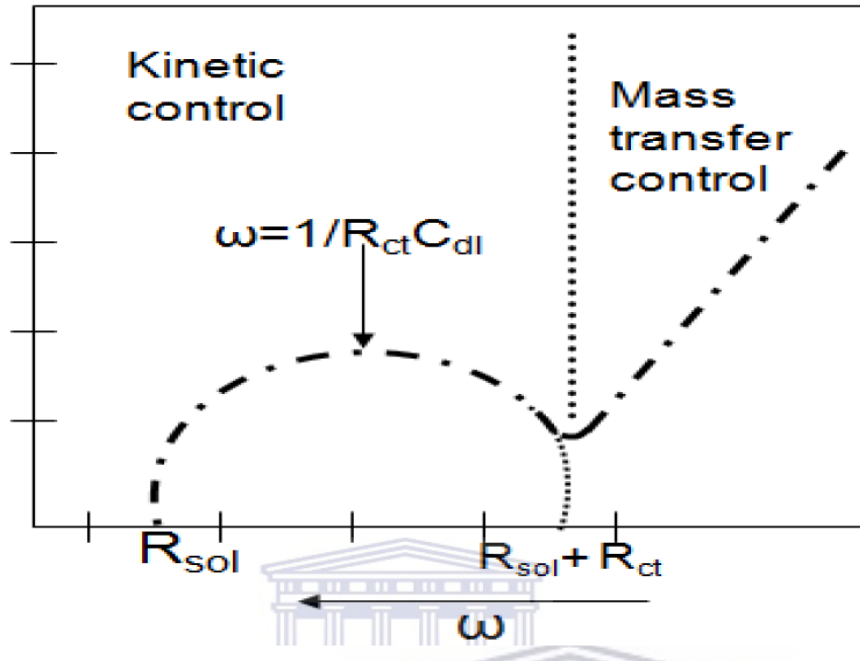
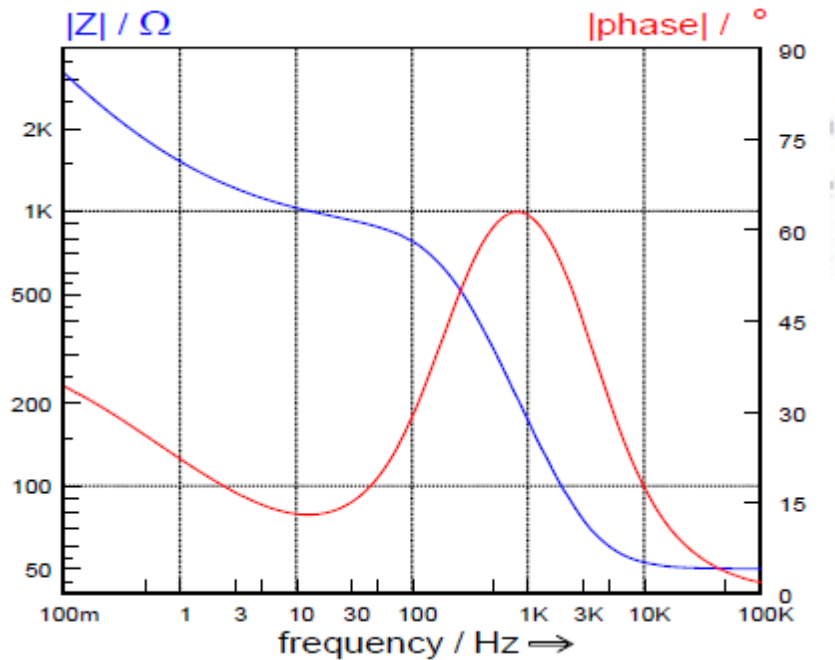Figure 13: A representative example of a typical nyquist plot indicating kinetic and mass control parameters

Figure 14: A representative example of a Bode plot

35

3.4   Methodology

3.4.1   Synthesis of LiMn₂O₄

In the Synthesis of nano-LiMn$_2$O$_4$ cathode material, the precursor spinel LiMn$_2$O$_4$ was prepared following a procedure found in the literature with minor adjustments. In a typical process, a stoichiometric amount of LiOH and Mn(CH$_3$COO)$_2$·4H$_2$O with cationic ratio of Li/Mn = 1:2 were dissolved in deionized water and mixed well by stirring gently. The solution is evaporated at 100 °C for 10 h to obtain the precursor powder. The precursor was further preheated at 400 °C for 1 h, and then subjected to calcinations at 800 °C for 20 h in a muffle furnace to form LiMn$_2$O$_4$ as illustrated in Figure 15 below [15].

3.4.2   Synthesis of AlF₃

Aluminium trifluoride, AlF$_3$, nanoparticles were obtained after calcinations of commercial Aluminium fluoride trihydride at 550 °C.
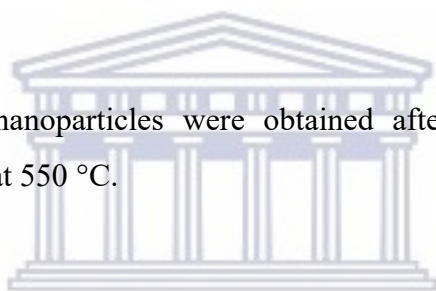
3.4.3   Synthesis of Carbon-Based Support Materials: Graphene

The synthesis of graphene was conducted using the Hummer method. In a typical process, 50 ml of concentrated H$_2$SO$_4$ was added into a 250 ml flask filled with 20 g of graphite powder at room temperature. The flask was cooled to 0°C in an ice bath followed by a slow addition of 7g KMnO$_4$. The flask was then allowed to warm to room temperature. The flask was then removed from the ice bath and the reaction temperature was allowed to rise to 35°C. The reaction mixture was stirred with a Teflon coated magnetic stirrer for 2 hrs, after which, it was cooled in an ice bath and 120 ml of H$_2$O was added as well as a slow addition of H$_2$O$_2$. The resulting suspension was extensively washed and centrifuged to remove residual unexfoliated graphite. The material obtained was vacuum dried at 65°C overnight to graphene oxide. 100 mg of graphene oxide was dispersed in 100 ml of H$_2$O and sonicated for 1 hr. This was followed by addition of 200 mg of NaBH$_4$ to the dispersion. The mixture was stirred for 30 min and heated under reflux at 142°C for 3 hrs (during

36

the reduction process, the yellow solution gradually yielded a black precipitate). The black solid was isolated by centrifugation, washed with water and finally dried [67].

3.4.4   Preparation of [LiMn$_{1.98}$O$_{3.99}$AlF$_{0.02}$ –rGO] nanocomposite

The novel nanocomposite cathode material was assembled in a 100 ml round bottomed flask in ethanol. After 24 hr mixing in ethanol at room temperature, the composite precipitate was collected in a crucible and calcined at 300 °C for 6 hr to produce[AlF$_3$LiMn$_2$O$_4$-rGO] nanocomposite. Figure 8 below is the schematic representation of the route employed in the synthesis of the [LiMn$_{1.98}$O$_{3.99}$AlF$_{0.02}$ –rGO] cathode composite.

3.4.5   Glassy carbon electrode preparation (LiMn$_2$O$_4$/GCE and [AlF$_3$LiMn2O$_4$-rGO]/GCE)

Electrochemical studies were carried out using a three-electrode system. The cathode was prepared by making a paste comprising of 70 wt% of active oxide material, 10 wt% of rGO and 20 wt% AlF$_3$ in 1-methyl-2-pyrrolidinone (NMP) to form a uniform catalytic solution. The slurry (5 µl) was prepared comprising of 2 mg/0.5 ml dropped onto a glassy carbon electrode and left to dry at room temperature overnight. The electrolyte used was a solution of 1 M LiNO$_3$ in a 1:1 (molar ratio). To determine the electrochemical reactions, present for the spinel cathode material in the potential range of -1.2 to 1.2 mV vs. Ag/AgCl reference electrode. All the experiments were recorded at ~ 25 °C and carried out in an argon atmosphere. The synthetic flow diagram of the novel [AlF$_3$LiMn$_2$O$_4$-rGO] can be seen in Figure 15.
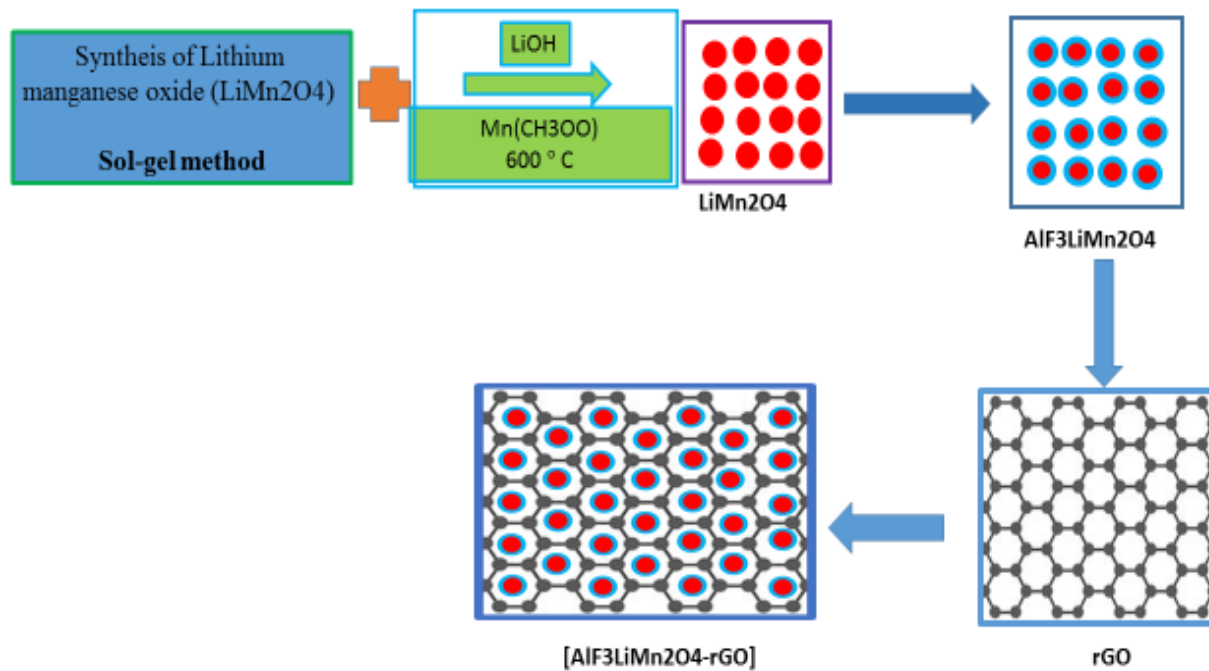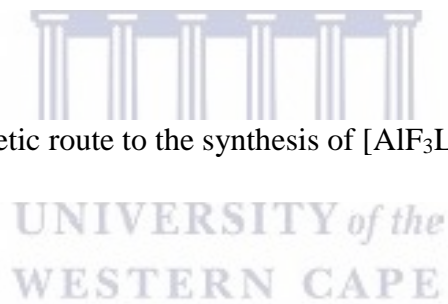
Figure 15: The synthetic route to the synthesis of [AlF$_3$LiMn$_2$O$_4$-rGO]

Chapter 4: Results and Discussion

Chapter Overview

This chapter outlines the results obtained for the pristine $LiMn_2O_4$ and novel $[AlF_3LiMn_2O_4\text{-}rGO]$ Li-ion cathode material. These include spectroscopic characterization techniques

4.1 Raman spectroscopy

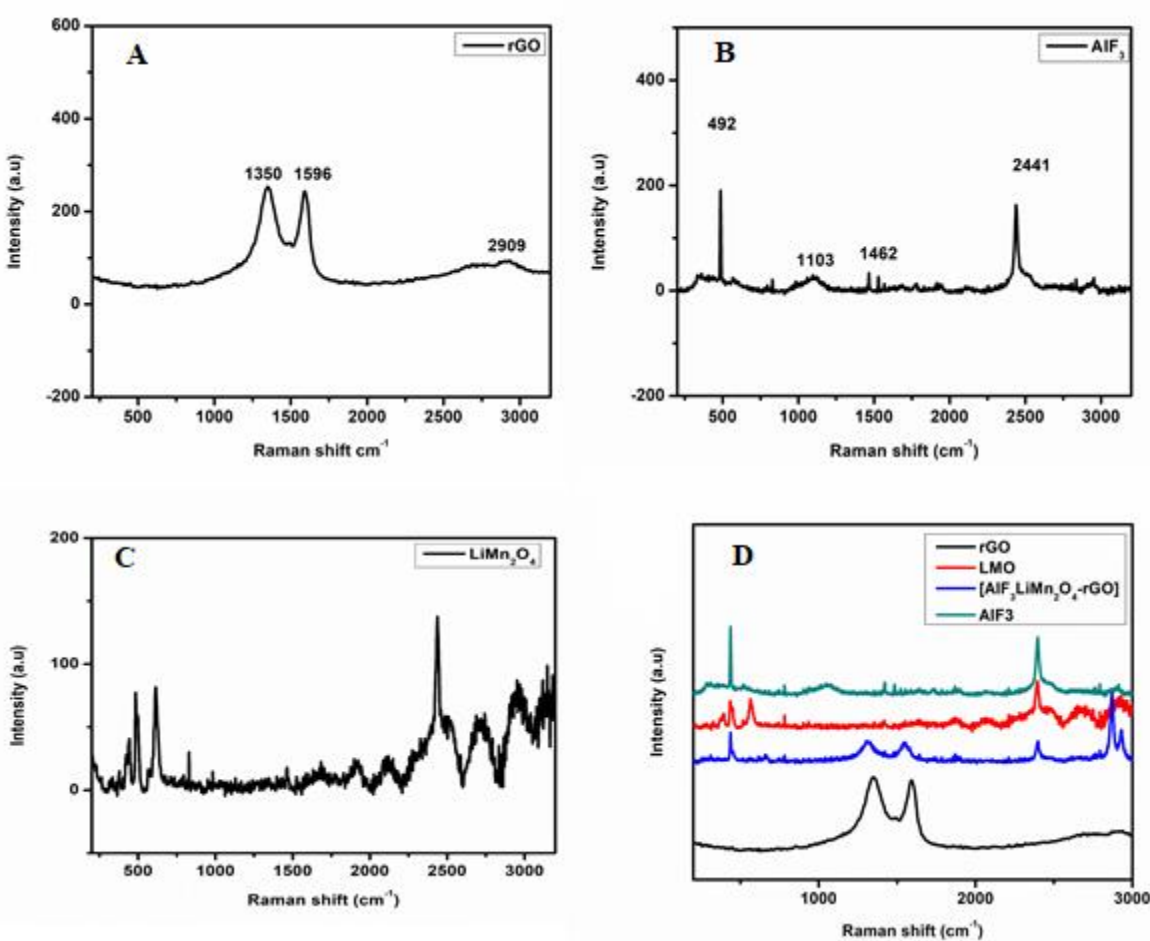Figure 16: Raman spectra of rGO, AlF_3, $LiMn_2O_4$ and Overlay raman plots

The vibrational information of the $LiMn_2O_4$ pristine cathode material is given by raman analysis of the octahedral MnO_6 and tetrahedral LiO_4 sublattice of spinel $LiMnO_4$. This raman spectra for $LiMn_2O_4$ is found in the spectral region in Figure 16 (A) found above. The most intense peak around 500 cm^{-1} is characteristic for pristine $LiMn_2O_4$ and also confirms that the spinel structure

was formed as was observed in XRD analysis. The strongest peak is assigned to A^{1g} mode which corresponds to Mn-O stretching vibration of the MnO_6 group [68].[69]. The raman spectrum of $LiMn_2O_4$ obtained also shows that the sample is related to the *Fd3m* space group.

The composite [$AlF_3LiMn_2O_4$-rGO] in Figure 16 (D) has more intense raman active bands than that of the pristine $LiMn_2O_4$. This could mean that the crystal structure is more stable and will allow for more charge/discharge cycles as insertion/extraction of Li-ions take place without capacity fading as can be seen in the pristine material. The band at 608 cm^{-1} is attributed to the A_{1g} mode which is characteristic for Mn-O stretching [70]. The band at 492 cm^{-1} is representative of the $t_{2g}(3)$ mode. The other bands in the region are weak and can be ascribed to the $t_{2g}(1)$ and $t_{2g}(2)$ modes. The bands in the region of 1370-1600 cm^{-1} can be ascribed to D and G bands of rGO which now forms part of the composite cathode material [71]. The D band at 1370 cm^{-1} represents the disorder of the sp^3 carbon atoms within the complex graphene structure and the G-band at 1600 cm^{-1} is representative of the structural superiority due to the sp^2 hybridized carbon atoms within the graphene lattice. The band vibration at 2432 cm^{-1} is a result of the gel used in sample preparation. The formation of the composite material gives rise to new intense peaks at 2917 and 2960 cm^{-1} respectively.
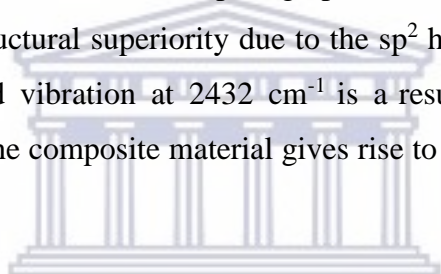
4.2 X-ray diffraction (XRD)
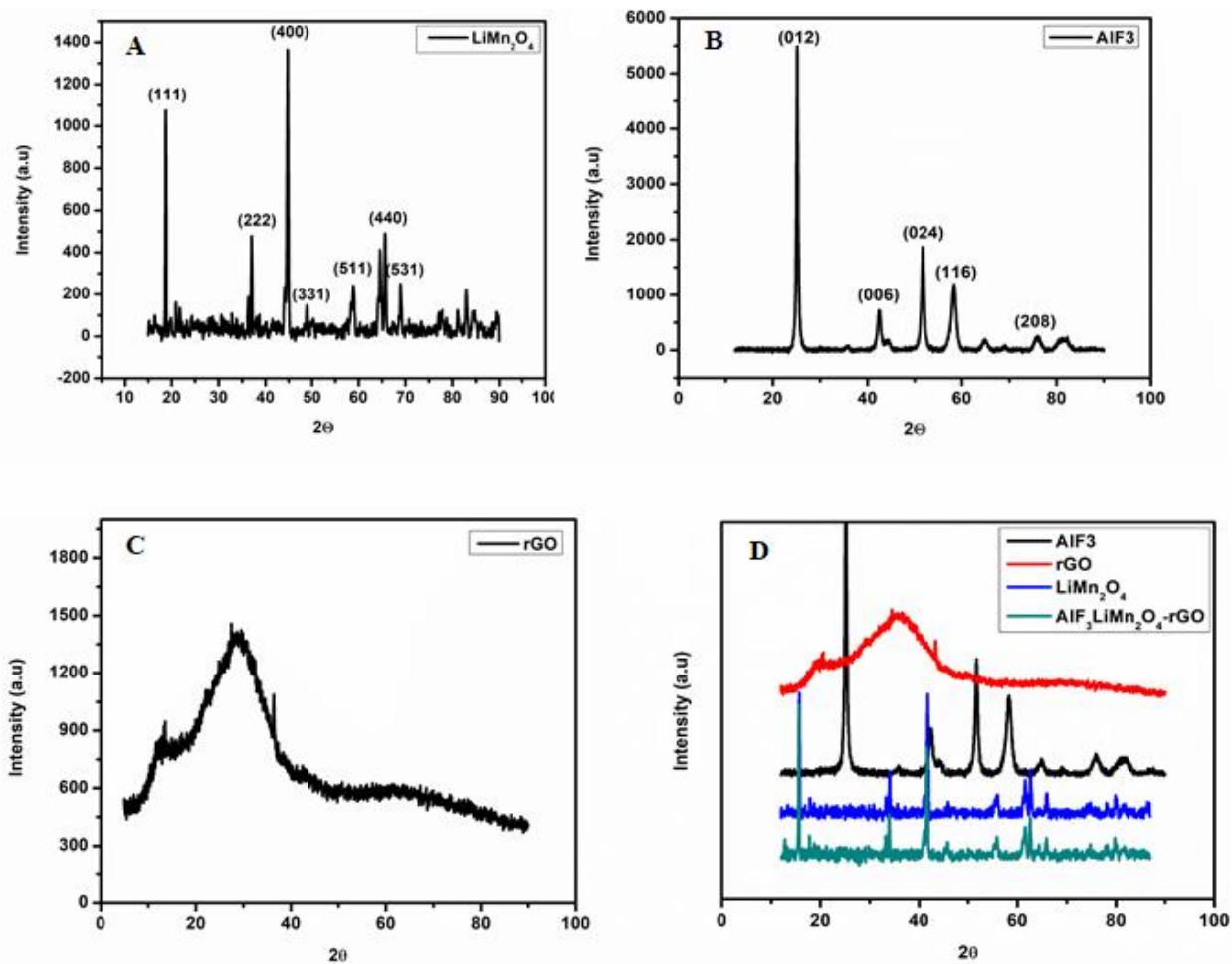
Figure 17: XRD plots of (A) LiMn$_2$O$_4$, (B) AlF$_3$, (C) rGO and (D) Overlay with AlF$_3$LiMn$_2$O$_4$ nanocomposite

The powder XRD pattern of pristine LiMn$_2$O$_4$ cathode material calcined at 800 °C is shown in Figure 17 (A) above. The indexed material synthesized has a face centered cubic (FCC) lattice, and an *Fd3m* space group. This structure allows for closely packed oxygen atoms in the Face centered cubic (FCC) unit cell which can be filled with 56 atoms [72]. The lithium ions occupy

41

the octahedral (8a) sites, the manganese the (16d) sites and oxygen the (32e) sites. The lattice parameter, a, as calculated from the least squares method is 8.24 Å [73]. This confirms that the spinel $LiMn_2O_4$ was formed. The high intensity of the (111) peak indicates good electrochemical activity for lithium ion batteries [74]. The narrow peaks observed, indicated that the material is crystalline and contains no impurities [75]. The XRD representation of AlF_3 in Figure 17 (B) above was obtained from the thermal treatment of commercial $AlF_3 \cdot 3H_2O$ at 450 ℃. Crystalline trigonal *alpha*-AlF_3 formed after air calcination and there is no indication of hydroxide species [60]. The spectrum above indicates that bulk AlF_3 is stable at elevated temperatures. The material can now be used as a catalytic coating material in Li-ion battery applications [60]. Amorphous rGO was obtained and is represent in figure (C) as a broad phase.

The bulk structure of the novel [$AlF_3LiMn_2O_4$-rGO] composite material is comprised of 70 % weight of the $LiMn_2O_4$ active cathode material, 20 % weight AlF_3 and 10 % rGO. From the XRD spectrum in Figure 17 above, it is clear that the novel material had no structural effect on the pristine $LiMn_2O_4$. The spinel remains unchanged. Li-ion insertion/extraction will therefore still take place, and more efficiently too as the coated Li-ions will withstand structural damage caused at elevated temperatures and increased cycle numbers. The specific capacity and energy density will therefore be improved.

Table 2: Comparison of Crystal structure, d-spacing and lattice constants of various material synthesized.

Material	Crystal structure	Lattice constant (a)	d-spacing (nm)
$LiMn_2O_4$	FCC	8.2476	0.22
AlF_3	Trigonal	4.9278	0.11
[$AlF_3LiMn_2O_4$-rGO]	FCC	8.2900	0.24

Table 2 above shows that the crystal lattice d-spacing of all materials synthesized. The crystal structure of the novel [$AlF_3LiMn_2O_4$-rGO] comparable to the pristine $LiMn_2O_4$ cathode material. The slight shift of 0.2 Å is also observed in the XRD spectrum and has a negligible effect on crystal structure.

http://etd.uwc.ac.za
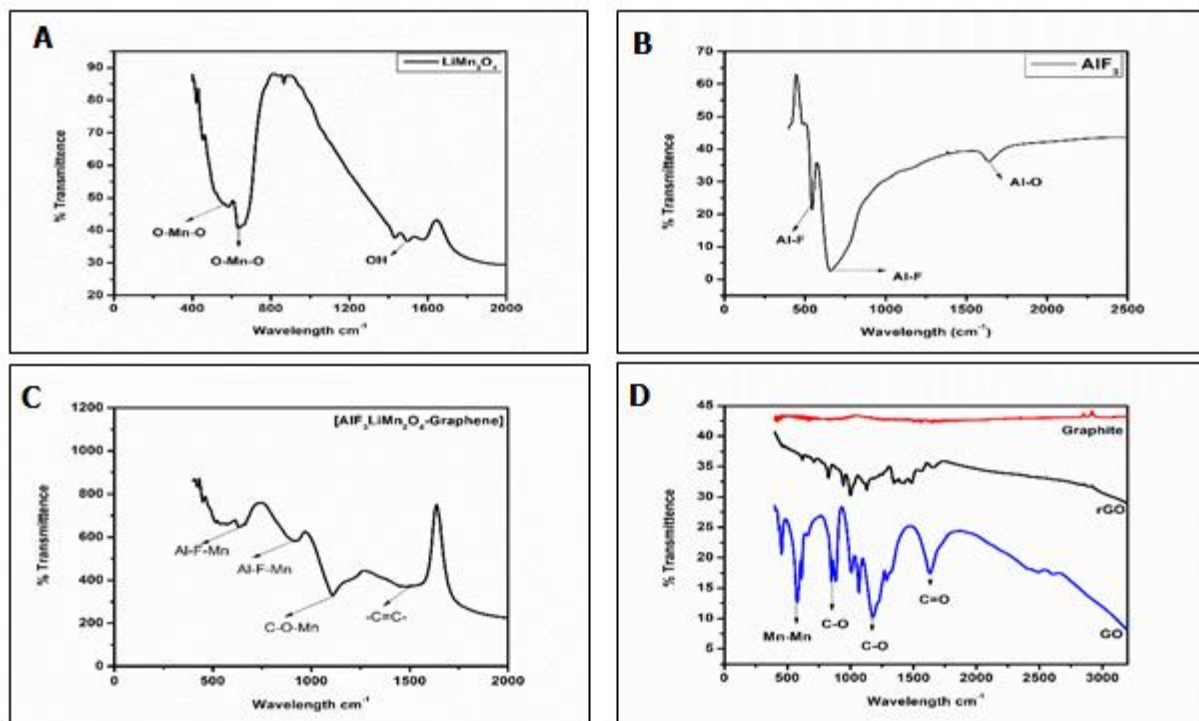
4.3 Fourier transfer infrared spectroscopy (FTIR)

Figure 18: FTIR plot of (A) LiMn$_2$O$_4$, (B) AlF$_3$, (C) [Graphite, rGO and GO overlay], (D) [AlF$_3$LiMn$_2$O$_4$-rGO]

(A) above shows infrared vibrational spectrum of pristine LiMn$_2$O$_4$. The strong bands at 640 and 578 cm^{-1} are characteristic to the formation of LiMn$_2$O$_4$. They are assigned to the asymmetric stretching of MnO$_6$ in the spinel structure. The shoulder ripple bands in the region of 1400 cm^{-1} are due to Mn-OH vibrations [76]. Figure 18 (B) above shows Al-F vibrations as well as the AlF$_3$ stability to oxygen moisture. There is a strong clearly separated broad peak at 655 cm^{-1} which can be assigned to the Al-F stretch [77]. This confirms that the AlF$_3$ is an amorphous material [78]. According to Roodenko *et al.*, the absorption band at 1644 cm^{-1} can be assigned to Al-O vibrations. This is however negligible due to its small intensity [78]. The Fourier transfer infrared (FT-IR) spectra of (a) Graphite, (b) rGO and (c) GO is observed in Figure 18 (C) above. From graphite, there are no distinct IR bands due to the fact that graphite has no functional groups attached to the carbon atoms. In (c) GO showed a collection of IR bands which correspond to; aromatic C=O (1644 cm^{-1}), alkoxy C-O (1180 cm^{-1}), C-O (862 cm^{-1}) and Mn-O (570 cm^{-1}). The observable functional groups that arise from the chemical oxidation of graphite by Potassium permanganate

43

(KMnO$_4$) gives a wide range of strong and weak IR bands as expected, also a Mn-O vibration is observed at 570 cm^{-1} this is due to the fact that Mn is a precursor material. Sodium borohydride (NaBH$_4$) was used as the chemical reducing agent of GO. In Figure (b), the reduced GO (rGO) product is clearly observed with less functional groups and has less intense bands. The bulk functional groups have therefore been removed from GO to form rGO [79].

The FTIR vibrational spectrum of the novel cathode material is observed in Figure 18 (D) above. There is an overlap which can be seen in the Al-F and Mn-O around 600 cm^{-1} which was expected and gives rise to the formation to vibrational modes of [AlF$_3$LiMn$_2$O$_4$-rGO]. A new band is observed in the 900 cm^{-1} region and is also assigned to Al-Mn-F stretches. A strong band is observed around 1100 cm^{-1} and is assigned to C-O-Mn vibrations. At 1504 cm^{-1} a broad -C=C- band confirms the presence of rGO in the novel cathode material.

4.4   Scanning electron microscopy (SEM)
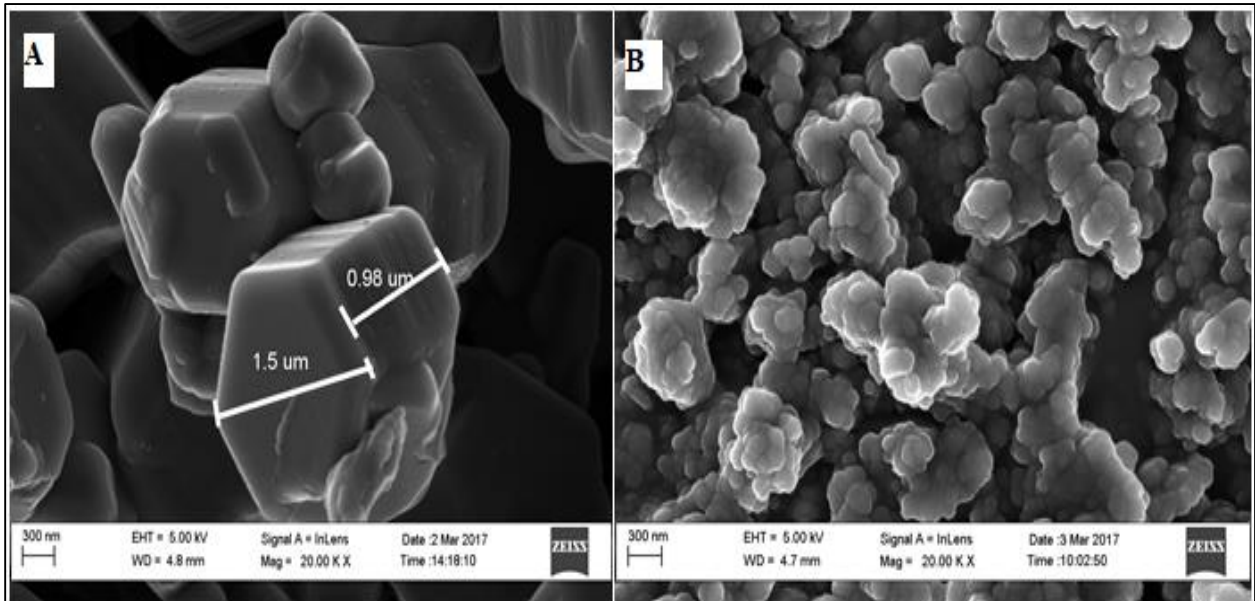
Figure 19: SEM micrograph of pristine (A) $LiMn_2O_4$ cathode material and (B) [$AlF_3LiMn_2O_4$-rGO] at a scale view of 300 nm and EDX spectrum with percentage weight proportions.

Element	Wt%	Wt% Sigma
O	27.95	0.52
Mn	72.05	0.52
Total:	100	
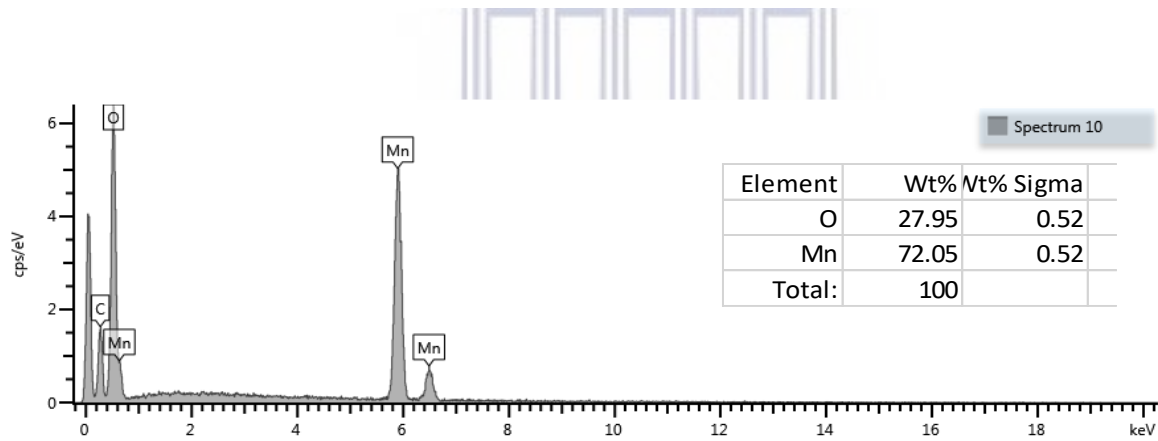
Figure 20: EDX Spectrum of $LiMn_2O_4$ and weight percentage

Figure 21: SEM micrograph of (A) AlF₃ and (B) rGO at a scale view of 200 nm and EDX spectrum with percentage weight proportions.

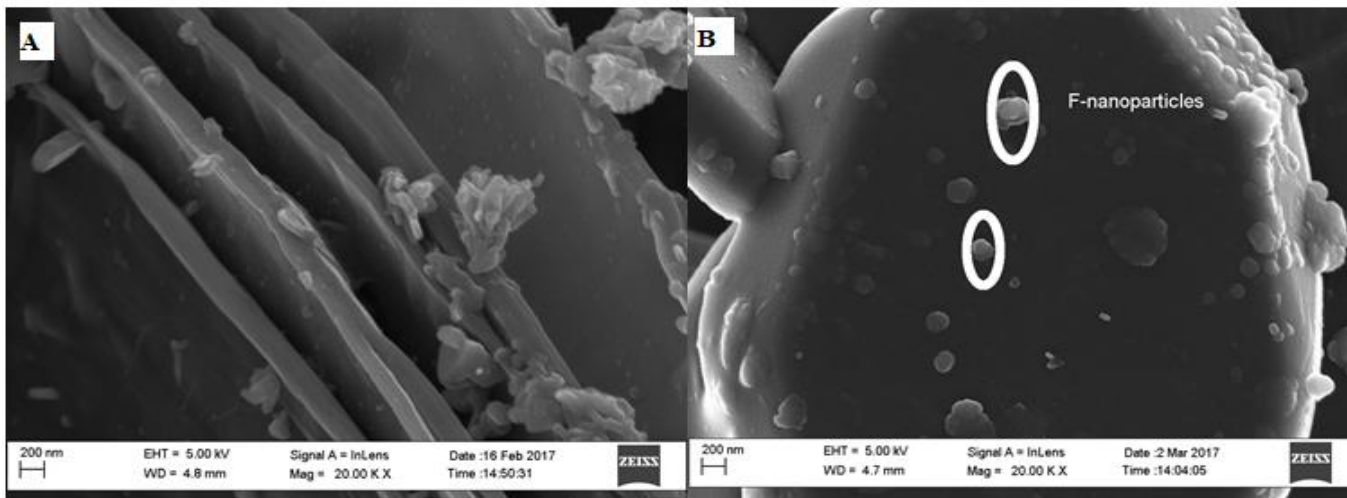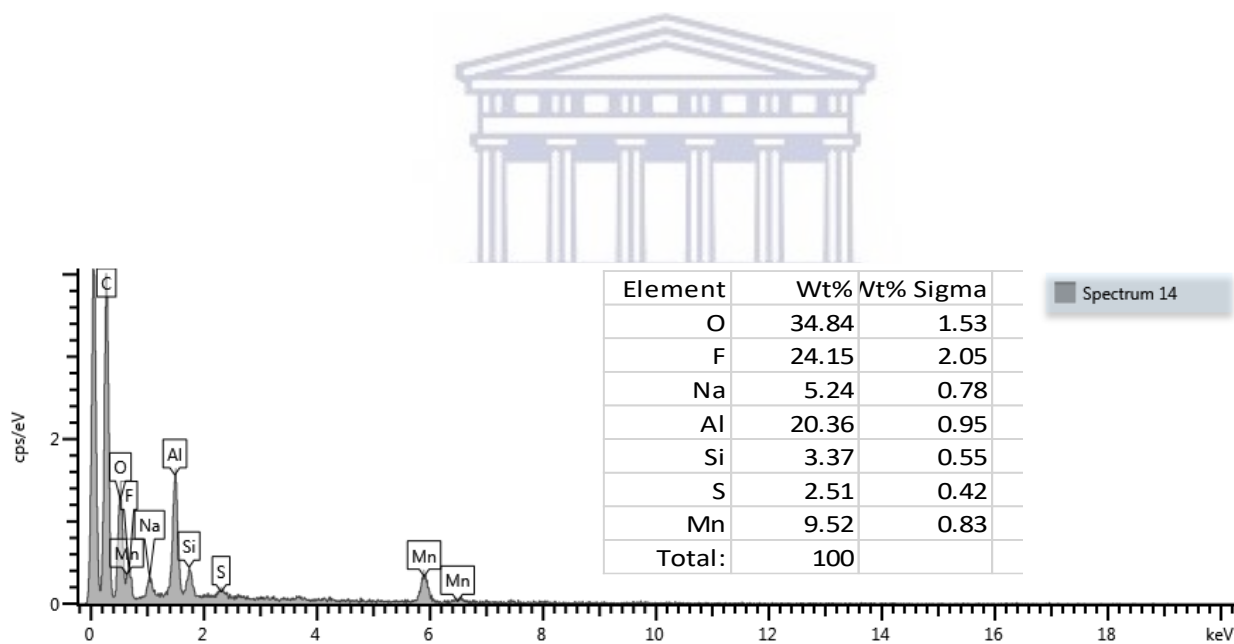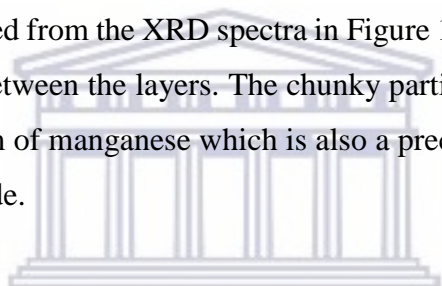| Element	Wt%	Wt% Sigma
O	34.84	1.53
F	24.15	2.05
Na	5.24	0.78
Al	20.36	0.95
Si	3.37	0.55
S	2.51	0.42
Mn	9.52	0.83
Total:	100	

Figure 22: EDX Spectrum of [AlF3LiMn2O4-rGO]

The SEM micrograph of $LiMn_2O_4$ in Figure 21 above shows that octahedral crystals which are well defined. Cubic particles were formed with the characteristic spinel shape. The carbon peak in the EDX spectrum is attributed to the coating used in the sample preparation step. The microscope used is not sensitive to lithium, hence we don't see lithium in the EDX spectrum, Lithium is however confirmed to be included in the metal oxide complex as is seen in the XRD and FTIR spectra in Figure 17 and Figure 18 . The observable particle in the SEM micrograph is in the micron range. Particle sizes within the $LiMn_2O_4$ spinel do however differ. The SEM micrograph of $LiMn_2O_4$ in Figure 19 A above shows that octahedral crystals which are well defined. The spinel in still maintained in the $[AlF_3LiMn_2O_4$-rGo] cathode composite formed. Particle sizes do vary, but their growth within the crystal lattice is impressive. There is also a small percentage of observable impurities found in the novel material. These are precursor materials which were used and are negligible in the overall electrochemical functioning or structural properties of the cathode material, the can also be observed from the XRD spectra in Figure 17. Graphene sheets can clearly be seen as there is separation between the layers. The chunky particles on top and in between the sheets are impurities in the form of manganese which is also a precursor material in the synthesis of graphene from graphene oxide.

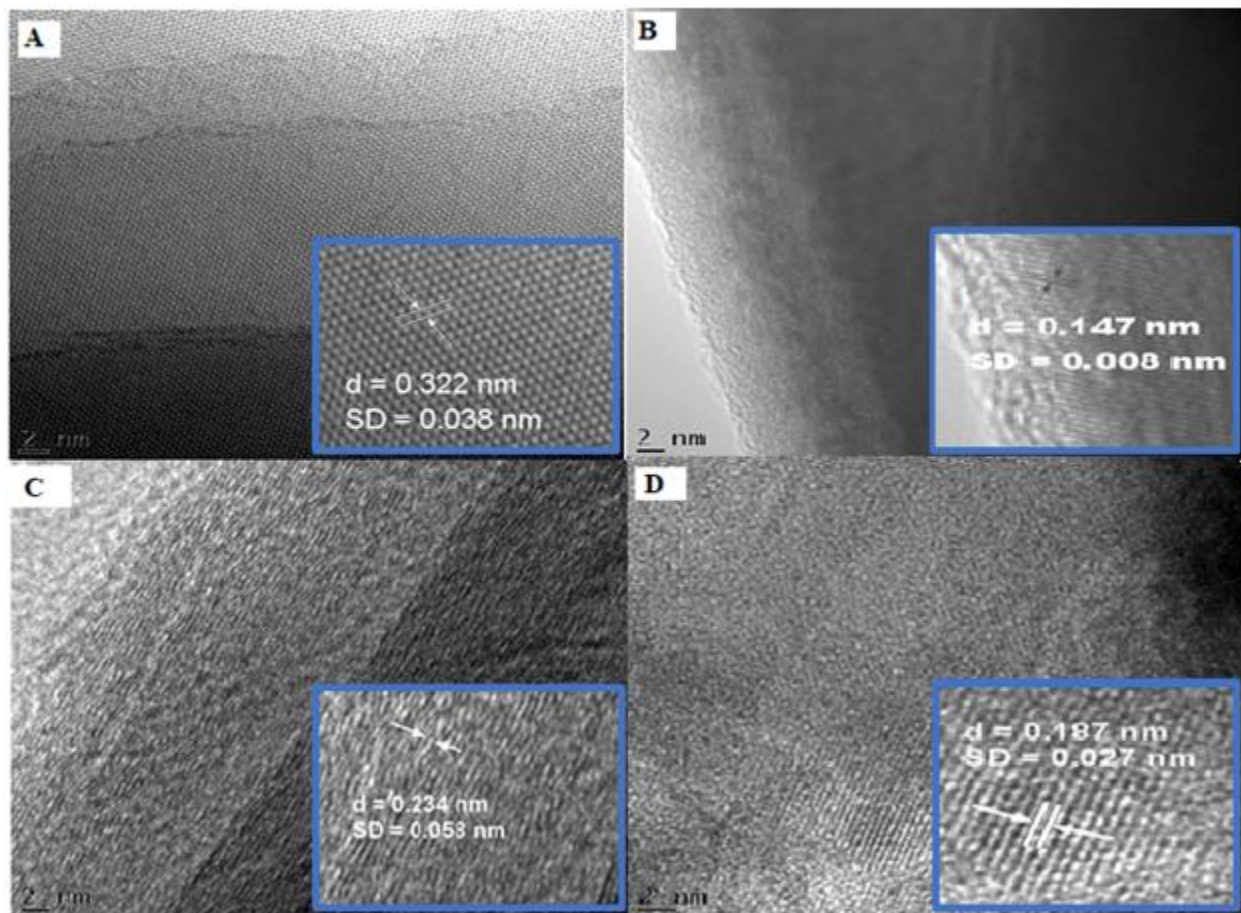## 4.5   High Resolution Transmission electron microscopy (HRTEM)

Figure 23: TEM micrographs of (A) $LiMn_2O_4$, (B) AlF_3, (C) rGO and (D) [$AlF_3LiMn_2O_4$-rGO] at a scale view of 2 nm

From the HRTEM micrographs in Figure 23 above, well developed lattice fringes are observed from all the materials. This indicates good crystallinity of the pristine cathode material (A) with a d-spacing separation value of d = 0.322 nm in the bulk region[15]. This value is comparable to the d-spacing value obtained from the (111) in the XRD spectrum of $LiMn_2O_4$ of 0.476 nm. SD is the standard deviation in the d-spacings obtained for the material. The AlF_3 (B) coating material shows superior d-spacing as compared to the pristine $LiMn_2O_4$ cathode material. This will allow for an improved modified cathode composite material which will display improved structural and electrochemical properties. The lattice fringes in the modified $LiMn_2O_4$ cathode material shows significant improvement in the d-spacing separation value (d = 0.187 nm) as compared to the

pristine material (A). This suggests that the modified material will display improved lithium diffusion properties, as the Li$^+$ path length is shorter for the charge/discharge process.

Chapter 5: Electrochemical characterization

Chapter Overview

Included in this chapter is the electrochemical analysis which was used to determine the redox reactions taking place on the surface of the GCE electrode as well as the capacity and diffusion capabilities of the novel [AlF$_3$LiMn$_2$O$_4$-rGO] cathode material. The techniques used were cyclic voltammetry, square wave voltammetry and electrochemical impedance spectroscopy (EIS)
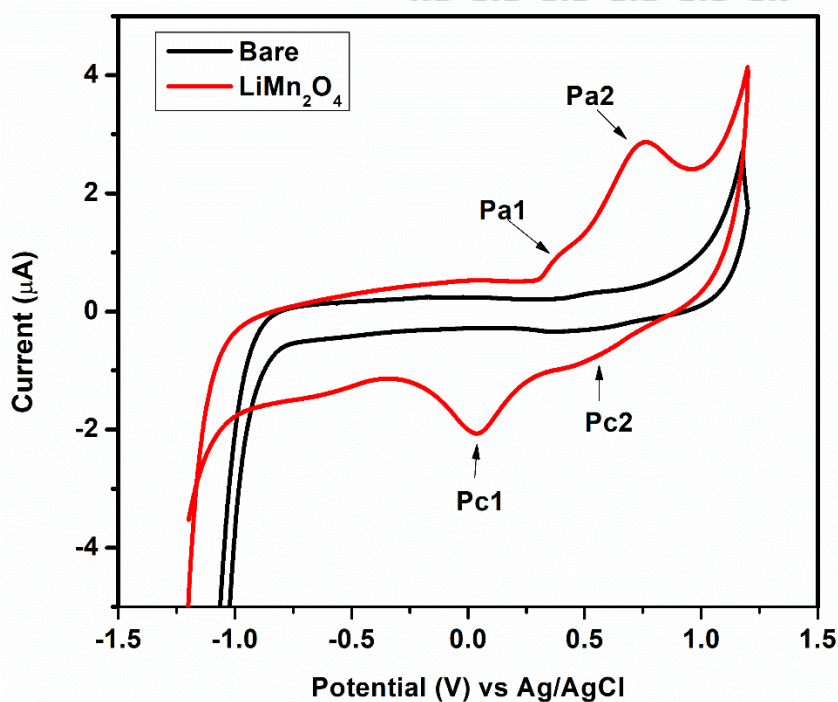
5.1   Cyclic Voltammetry

Figure 24: CV of LiMn$_2$O$_4$ and bare electrode in 1 M LiNO$_3$

Figure 24 above shows the CV overlay of the bare GCE with $LiMn_2O_4$ in 1 M $LiNO_3$ electrolyte solution. The distinct $LiMn_2O_4$ peaks show that the pristine cathode material is conductive as it allows a current to pass through across a potential range of -1.2 to 1.2 V on Glassy carbon electrode (GCE) surface. The redox peaks at P_{a1}/P_{c1} represent the lithium ion insertion and extraction at half the lithium sites. The peaks at P_{a2}/P_{c2} represents the insertion/extraction of lithium ions at the unreacted sites within the spinel. This is characteristic of the 2-step reversible transformation which takes place between $LiMn_2O_4$ and λ-MnO_2[73]. Figure 25 below shows the CV overlay of $LiMn_2O_4$ between scan rates of 5- 40 $mV.s^{-1}$. The most prominent redox peaks are observed at a scan rate of 40 $mV.s^{-1}$ which gives rise to a current density of about 3 μA.
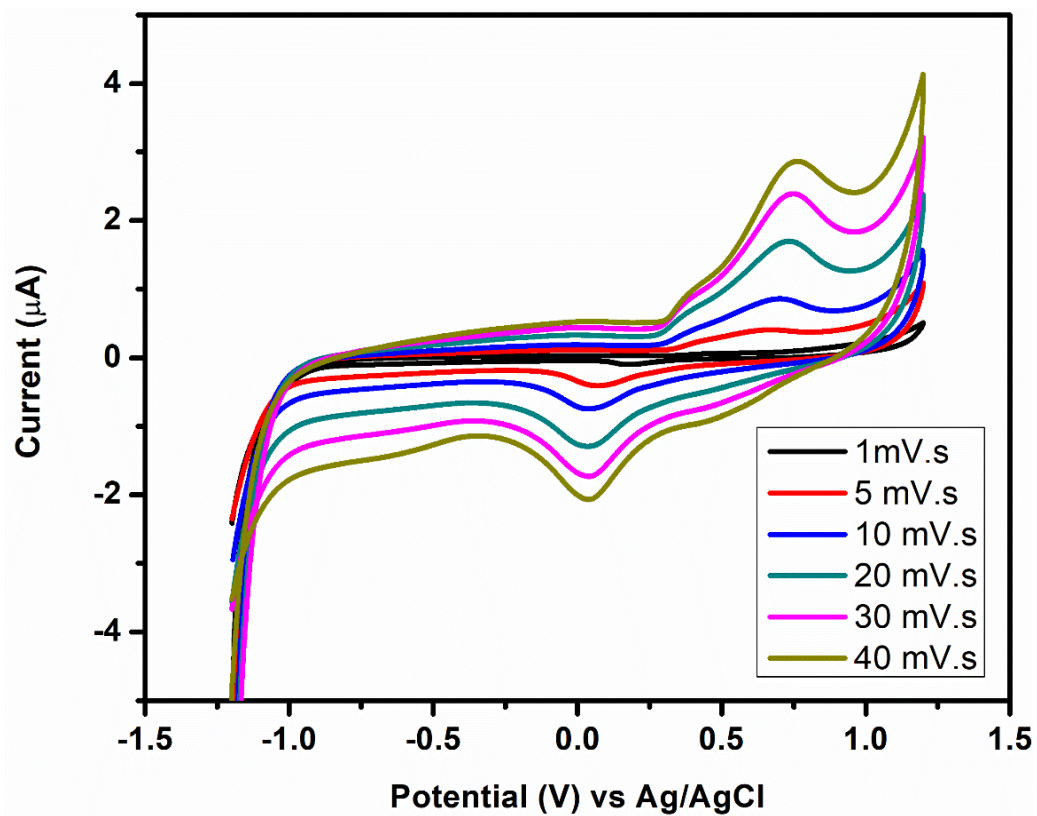
Figure 25: CV of LMO overlay between 5 and 40 $mV.s^{-1}$ in 1 M $LiNO_3$

Table 3: Parameters obtained from the CV of LiMn$_2$O$_4$

Scan Rate (mV.s^{-1})	Scan Rate$^{1/2}$ (mV.s^{-1})	I$_{pa}$ (µA)	I$_{pc}$ (µA)	E$_{pa}$ (V)	E$_{pc}$ (V)	ΔE$_p$ (V)
1	1	0.065	-0.092	0.52	0.17	0.35
5	2.24	0.39	-0.38	0.68	0.07	0.61
10	3.16	0.88	-0.74	0.70	0.04	0.66
20	4.47	1.73	-1.26	0.73	0.03	0.70
30	5.48	2.39	-1.68	0.76	0.04	0.72
40	6.32	2.89	-2.08	0.77	0.03	0.74
Mean				**0.69**	**0.06**	**0.63**

Figure 26: Plot of peak current vs root scan rate

Figure 26 shows that cathodic and anodic current density increases with increasing scan rate. The linear correlation shows that the pristine LiMn$_2$O$_4$ cathode material is conductive.

Determination of reversibility:

51

$$Ipa = Ipc \tag{38}$$

$$-\frac{I_{pa}}{I_{pc}} = -\frac{2.89 \ \mu A}{2.08 \ \mu A}$$

$$= 1.39 \ \mu A$$

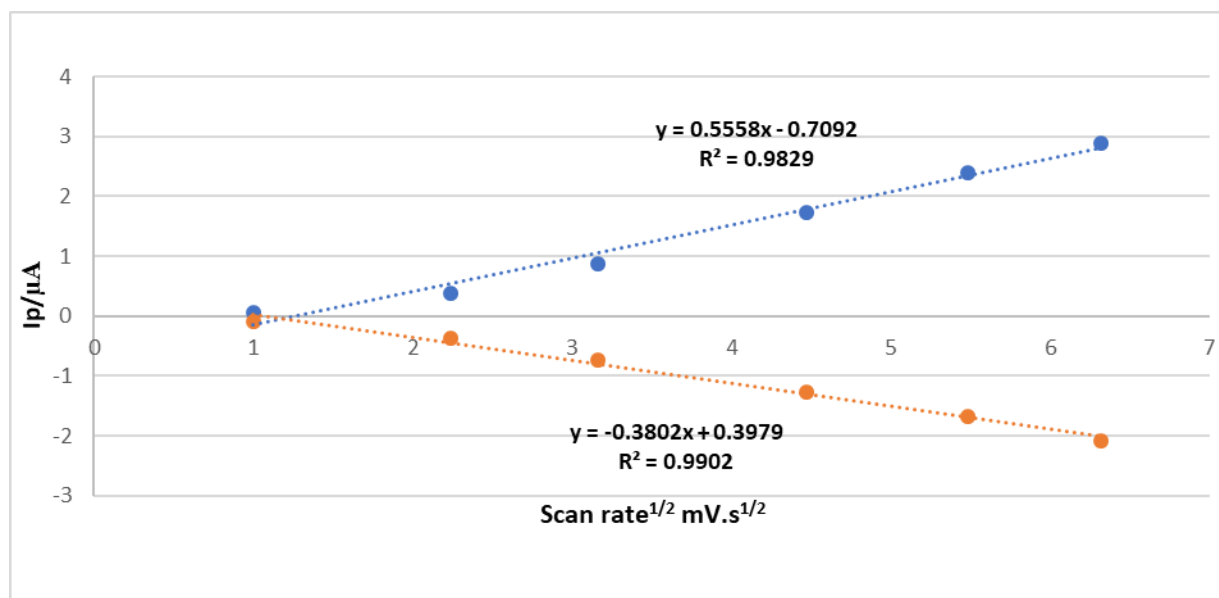$$\therefore -\frac{I_{pa}}{I_{pc}} \approx 1 \ ... \ \text{Chemically reversible}$$

Determination of Diffusion Coefficient:

$$Ipa = 0.4463nFA\left[\frac{nF}{RT}\right]^{\frac{1}{2}}[Ox]^{Bulk}Dox^{\frac{1}{2}}V^{\frac{1}{2}} \tag{39}$$

$$Slope = 0.4463nFA\left[\frac{nF}{RT}\right]^{\frac{1}{2}}[Ox]^{Bulk}Dox^{\frac{1}{2}} \tag{40}$$

$$Dox^{\frac{1}{2}} = \frac{Slope \ x \ (RT)^{1/2}}{0.4463(nF)^{\frac{3}{2}}A[Ox]^{Bulk}}$$

$$Dox^{\frac{1}{2}} = \frac{0.558x10^{-6}\ (\frac{s}{mV})^{\frac{1}{2}} \ x \ (8.314 \ J.mol^{-1}.K^{-1} \ x \ 298 \ K)^{1/2}}{0.4463(1 \ x \ 96485.33 \ C.mol^{-1})^{\frac{3}{2}} \ x \ 0.071 \ cm^{-1}[0.011 \ mol.dm^{-3}]}$$

$$D_{Li^+} = \left(2.65x10^{-9} \ cm.s^{-\frac{1}{2}}\right)^2$$

52

$$D_{Li^+} = 7.069 \ x \ 10^{-18} \ cm^2.s^{-1}$$

The diffusion corresponds to the 2 step process of extraction/ insertion of lithium ions in the spinel structure [80].

Determination of Specific Capacity for LiMn₂O₄ during charging

$$Q = \frac{\text{Area (AV)}}{\text{Scan rate (V.s}^{-1})} \tag{41}$$

$$Q = \frac{4.88 \text{x} 10^{-7} \text{AV}}{0.001 \text{ V.s}^{-1}}$$

$$Q = 4.88 \text{x} 10^{-4} \text{As}$$

Capacity units in batteries are in Amperes-hour. Since 3600 As = 1Ah

$$Q = \frac{4.88 \text{x} 10^{-4} \text{ A.s}}{3600 \text{ s}}$$

$$= 1.36 \text{x} 10^{-7} \text{A.h}$$

$$\text{Specific capacity}_{Charge} = \frac{Q \text{ (Ah)}}{\text{Active mass (g)}} \tag{42}$$

$$\text{specific capacity}_{Charge} = \frac{1.36x10^{-7} Ah}{8x10^{-4} \text{ g}}$$

$$1.69x10^{-4} Ah.\,g^{-1}x1000 \text{ mA}$$

0.17 mAh. g^{-1}

Determination of Specific Capacity for LiMn$_2$O$_4$ during discharging

$$Q = \frac{\text{Area (AV)}}{\text{Scan rate (V.\,s}^{-1})}$$

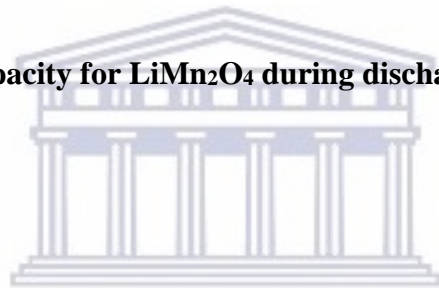$$Q = \frac{2.85x10^{-7} AV}{0.001 \text{ V.\,s}^{-1}}$$

$$Q = 2.85x10^{-4} As$$

$$Q = \frac{2.85x10^{-4} \text{ A.\,s}}{3600 \text{ s}}$$

$$= 7.91x10^{-8} A.\,h$$

$$\text{Specific capacity}_{Discharge} = \frac{Q \text{ (Ah)}}{\text{Active mass (g)}}$$

$$\text{specific capacity}_{\text{Discharge}} = \frac{7.91 \text{x} 10^{-8} \text{Ah}}{8 \text{x} 10^{-4} \text{ g}}$$

$9.90 \text{x} 10^{-4} \text{Ah. g}^{-1} \text{x} 1000 \text{ mA}$

$\mathbf{0.099 \text{ mAh. g}^{-1}}$

5.2 Cyclic voltammetry: [AlF₃LiMn₂O₄-rGO]

From the CV of [AlF$_3$LiMn$_2$O$_4$-rGO] in Figure 27 below, it is observed that the current density of the modified cathode material has improved. This is due to the influence of rGO which has superior electron conducting properties [16]. The modified cathode material will thus also have improved electrochemical properties. The Li-ion insertion/extraction peaks are not clear in the CV overlay in the figure above, we thus opted to use the more sensitive square wave voltammetry electrochemical characterization technique. In Figure 28 and Figure 29 below, we can confirm that lithium ion extraction/insertion does take place on the surface of the GC electrode. Table 5 below also shows the distinct capacitive improvements made between the pristine LiMn$_2$O$_4$ and novel [AlF$_3$LiMn$_2$O$_4$-rGO] cathode materials.
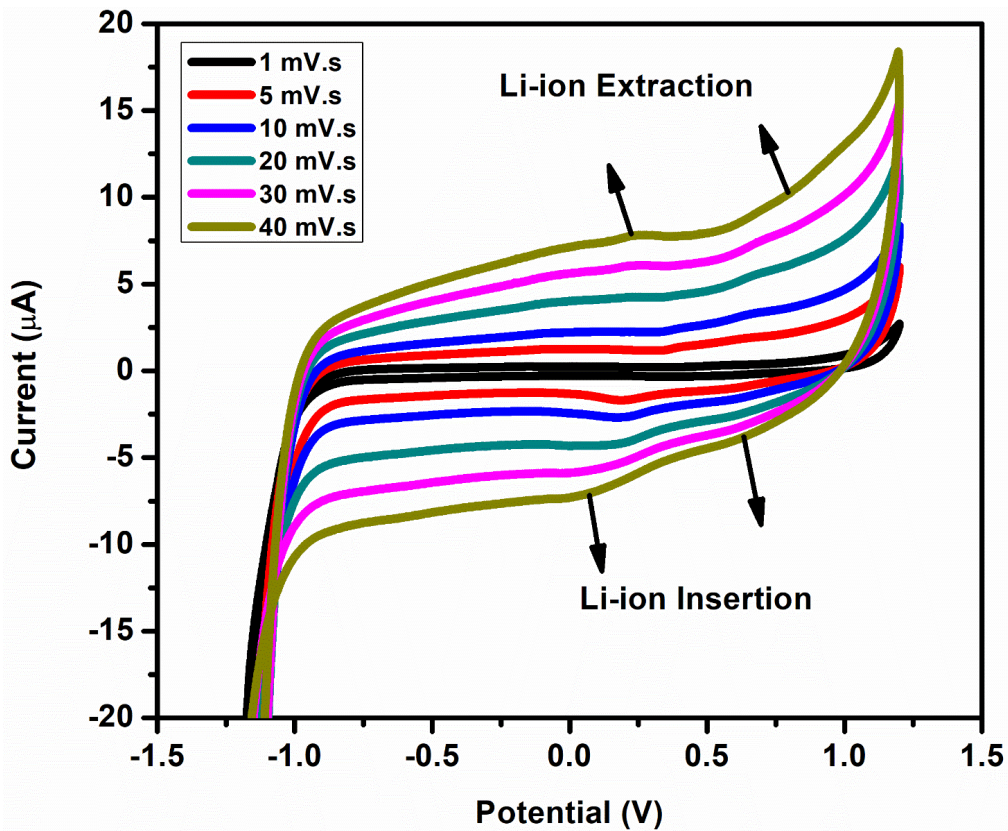
Figure 27: CV of [AlF$_3$LiMn$_2$O$_4$-rGO] overlay between 5 and 40 mV.s^{-1}
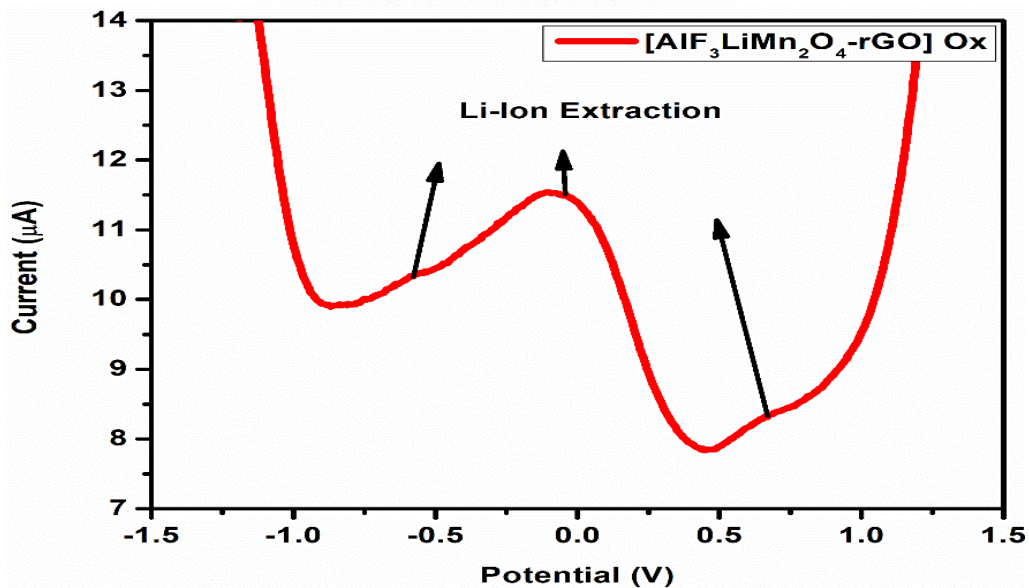
Figure 28: Anodic square wave voltammogram of [AlF$_3$LiMn$_2$O$_4$-rGO] in 1 M LiNO$_3$
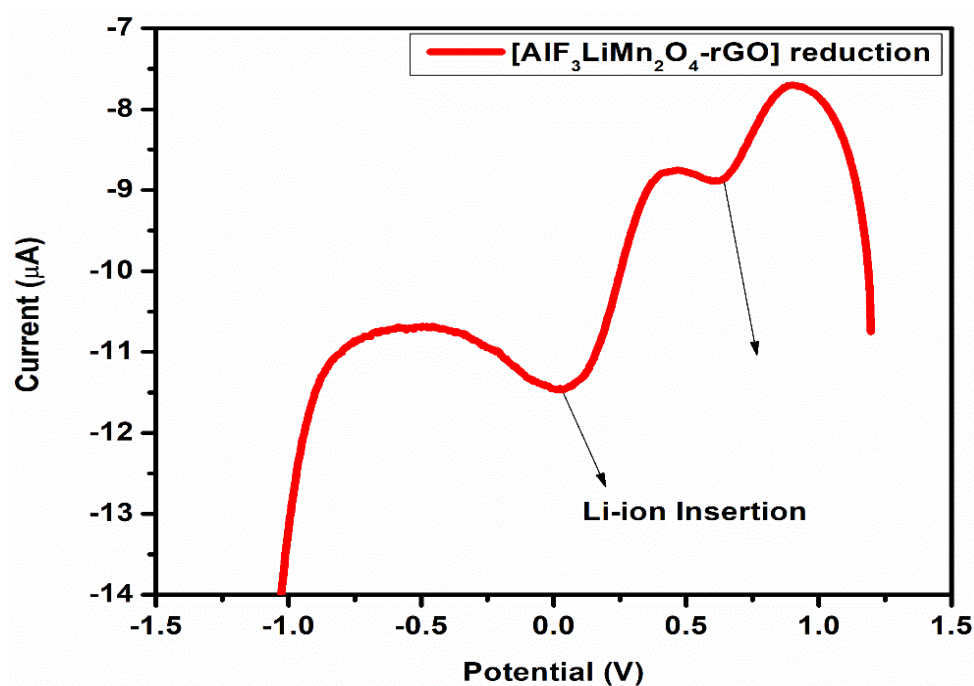
Figure 29: Cathode square wave voltammogram of [AlF$_3$LiMn$_2$O$_4$-rGO] in 1M LiNO$_3$

Table 4: Parameters obtained from the CV of [AlF$_3$LiMn$_2$O$_4$-rGO]

Scan Rate (mV.s^{-1})	Scan Rate$^{1/2}$ (mV.s^{-1})	I$_{pa}$ (µA)	I$_{pc}$ (µA)	E$_{pa}$ (V)	E$_{pc}$ (V)	ΔE$_p$ (V)
1	1	0.34	-0.34	0.57	0.37	0.20
5	2.24	1.94	-1.72	0.66	0.19	0.47
10	3.16	3.40	-2.71	0.69	0.19	0.50
20	4.47	5.63	-4.29	0.69	0.19	0.50
30	5.48	7.82	-5.60	0.72	0.13	0.59
40	6.32	10.14	-7.17	0.80	0.07	0.73
Mean				**0.69**	**0.19**	**0.50**

57
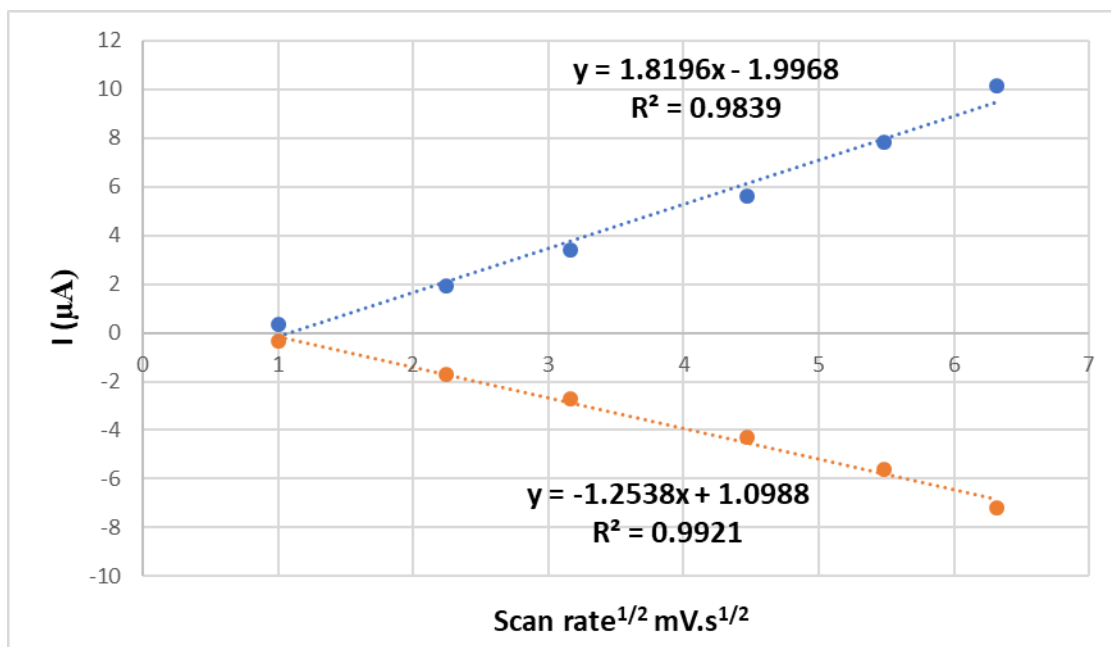
Figure 30: Plot of peak current vs root scan rate

Figure 30 above shows that cathodic and anodic current density increases with increasing scan rate. The linear correlation shows that the modified [AlF$_3$LiMn$_2$O$_4$-rGO] cathode material is conductive. From this plot it is easy to see that the current density of the modified cathode material is higher than that of the pristine cathode material (Figure 26) and promises improved electrochemical properties.

Determination of reversibility:

$I_{pa} = I_{pc}$

$$- \frac{I_{pa}}{I_{pc}} = - \frac{7.91 \ \mu A}{7.28 \ \mu A}$$

$= 1.09 \ \mu A$

$\therefore - \frac{I_{pa}}{I_{pc}} \approx 1 \ ...$ Chemically reversible

Determination of Diffusion Coefficient:

58

$$Ipa = 0.4463nFA \left[\frac{nF}{RT}\right]^{\frac{1}{2}} [Ox]^{Bulk} Dox^{\frac{1}{2}} V^{\frac{1}{2}}$$

$$Slope = 0.4463nFA \left[\frac{nF}{RT}\right]^{\frac{1}{2}} [Ox]^{Bulk} Dox^{\frac{1}{2}}$$

$$Dox^{\frac{1}{2}} = \frac{Slope \times (RT)^{1/2}}{0.4463(nF)^{\frac{3}{2}} A[Ox]^{Bulk}}$$

$$Dox^{\frac{1}{2}} = \frac{1.819 \times 10^{-6} \left(\frac{s}{mV}\right)^{\frac{1}{2}} \times (8.314 \, J.mol^{-1}.K^{-1} \times 298 \, K)^{1/2}}{0.4463(1 \times 96485.33 \, C.mol^{-1})^{\frac{3}{2}} \times 0.071 \, cm^{-1}[0.011 \, mol.dm^{-3}]}$$

$$D_{Li^+} = \left(8.67 \times 10^{-9} \, cm.s^{-\frac{1}{2}}\right)^2$$

$$\mathbf{D_{Li^+} = 7.52 \times 10^{-17} \, cm^2.s^{-1}}$$

The diffusion coefficient obtained for the modified cathode material ($D_{Li^+} = 7.52 \times 10^{-17} \, cm^2.s^{-1}$) is higher than that of the pristine material ($D_{Li^+} = 7.069 \times 10^{-18} \, cm^2.s^{-1}$) and therefore indicates that the process of Li^+ insertion/extraction on the surface of the electrode is improved [80].

Determination of specific capacity for [AlF₃LiMn₂O₄-rGO] during charging

$$Q = \frac{\text{Area (AV)}}{\text{Scan rate (V.s}^{-1})}$$

$$Q = \frac{3.39 \text{x} 10^{-6} \text{AV}}{0.001 \text{ V.s}^{-1}}$$

$$Q = 3.39 \text{x} 10^{-3} \text{As}$$

Capacity units in batteries are in Amperes-hour. Since 3600 As = 1Ah

$$Q = \frac{3.39 \text{x} 10^{-3} \text{ A.s}}{3600 \text{ s}}$$

$$= 9.42 \text{x} 10^{-7} \text{A.h}$$

$$\text{Specific capacity}_{\text{Charge}} = \frac{Q \text{ (Ah)}}{\text{Active mass (g)}}$$

$$\text{specific capacity} = \frac{9.42 \text{x} 10^{-7} \text{Ah}}{8 \text{x} 10^{-4} \text{ g}}$$

$$1.18 \text{x} 10^{-3} \text{Ah.g}^{-1} \text{x} 1000 \text{ mA}$$

$$\mathbf{1.18 \ mAh.g^{-1}}$$

Determination of specific capacity for [AlF₃LiMn₂O₄-rGO] during discharging:

$$Q = \frac{\text{Area (AV)}}{\text{Scan rate (V.s}^{-1})}$$

$$Q = \frac{3.46 \text{x} 10^{-6} \text{AV}}{0.001 \text{ V.s}^{-1}}$$

$$Q = 3.46 \text{x} 10^{-3} \text{As}$$

60

$$Q = \frac{3.46 \times 10^{-3} \, \text{A.s}}{3600 \, \text{s}}$$

$$= 9.61 \times 10^{-7} \text{A.h}$$

$$\text{Specific capacity}_{\text{Discharge}} = \frac{Q \, (\text{Ah})}{\text{Active mass (g)}}$$

$$\text{specific capacity}_{\text{Discharge}} = \frac{9.61 \times 10^{-7} \text{Ah}}{8 \times 10^{-4} \, \text{g}}$$

$$1.20 \times 10^{-3} \text{Ah.g}^{-1} \times 1000 \, \text{mA}$$

$$\mathbf{1.20 \; mAh.g^{-1}}$$

Table 5: Charge and discharge capacity for $LiMn_2O_4$ and $[AlF_3LiMn_2O_4\text{-rGO}]$

Cathode material	Charge capacity (mAh/g)	Discharge capacity (mAh/g)	Coulombic efficiency (%)	Capacity loss/gain (%)
Pristine LiMn₂O₄	0.17	0.099	58.24	41.76
Novel [AlF₃LiMn₂O₄	1.18	1.2	101.69	1.69

5.3 Electrochemical Impedance Spectroscopy (EIS)

EIS was used to investigate the intrinsic resistive and diffusion properties of the pristine $LiMn_2O_4$ and more importantly novel $[AlF_3LiMn_2O_4\text{-rGO}]$ as the redox activity taking place on the surface of the GCE in the electrochemical cell. The nyquist plots for $LiMn_2O_4$ and $[AlF_3LiMn_2O_4\text{-rGO}]$ are seen in Figure 31 below. No semi-circle region is observed, meaning that the electrode materials have good capacitive properties. The modified cathode material however, is steeper in the midfrequency range and therefore has less charge transfer resistance. This is also confirmed from the equivalent circuit modelling which was used to estimate its parameters seen in Figure 31 below [81]. The solution resistance of the novel cathode material has increased from 15 to 22 Ω.

This could be a result of the modified composite material being denser and hence the initial resistance is slightly higher than the pristine $LiMn_2O_4$ cathode material. The charge transfer resistance (R_{ct}) however, has decreased from 318 to 245.70 Ω, meaning that the modified cathode material is more conductive. This is confirmed from the bode plots below where the phase angle increased from 39.2 to 40.6° in

Figure 32 and Figure 33.
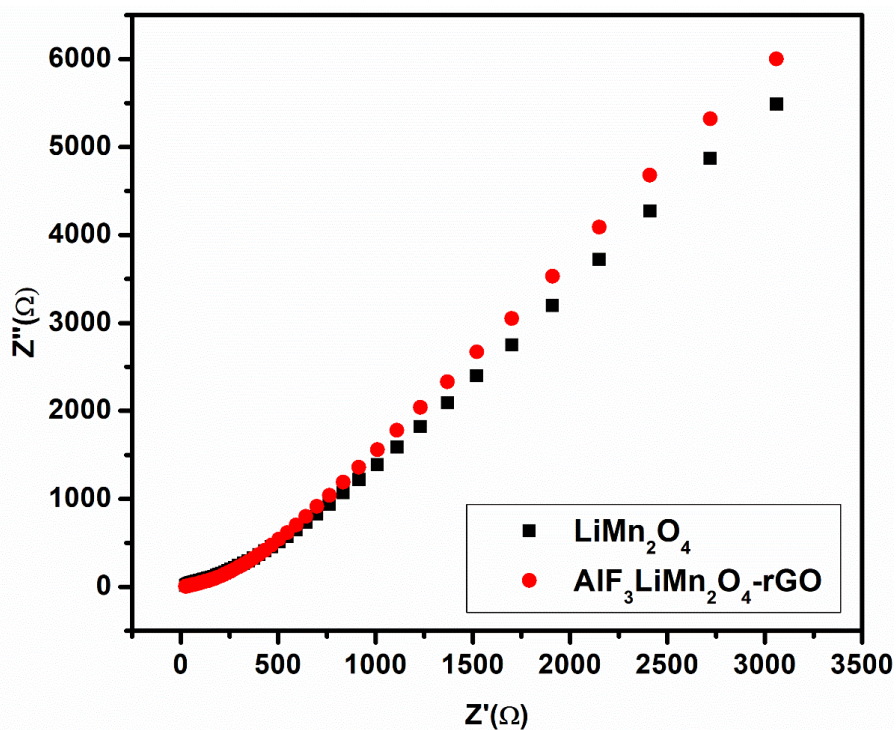
Figure 31: Nyquist plots for the pristine $LiMn_2O_4$ and $AlF_3LiMn_2O_4$ cathode GCE in 1M $LiNO_3$
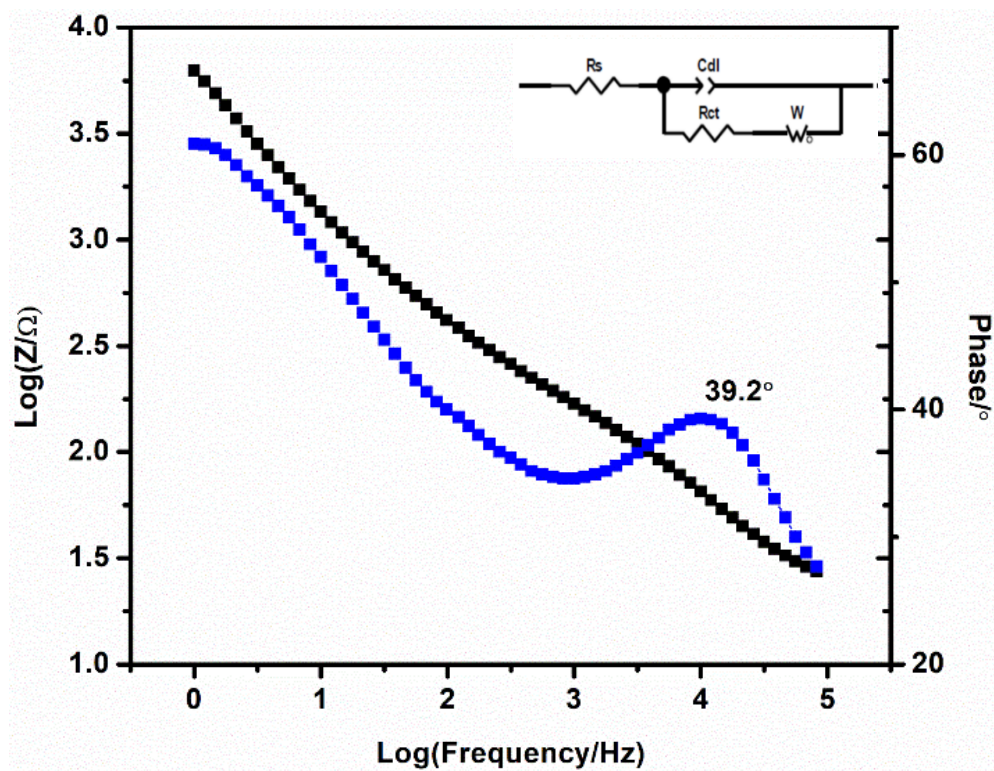
Figure 32: Bode plot for pristine LiMn$_2$O$_4$ cathode material obtained at a formal potential of 0.465 V in 1 M

Inset: Randle model describing the equivalent circuit
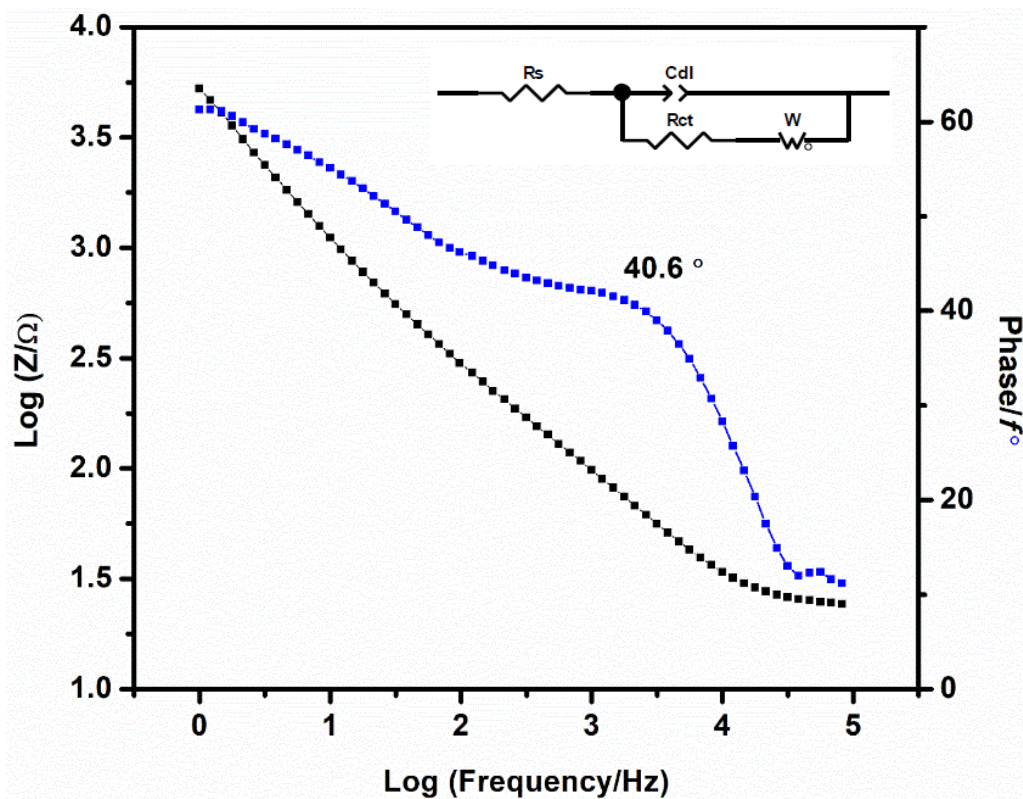
Figure 33: Bode plot for [AlF$_3$LiMn$_2$O$_4$-rGO] cathode material obtained at a formal potential of 0.1 V in 1 M LiNO$_3$.

Inset: Randle model describing the equivalent circuit

Table 6: Kinetic Parameters obtained from EIS plots

Electrode	R$_s$ (Ω)	C$_{dl}$(µF)	R$_{ct}$ (Ω)	W$_s$ (Ω/s$^{-1/2}$)	I$_0$
LiMn$_2$O$_4$	15.11	1.60x10^{-5}	318	1.03	8.07x10^{-5}
AlF$_3$LiMn$_2$O$_4$	22.27	1.39x10^{-5}	245.7	1.07	1.05x10^{-4}

64

$$i_o = \frac{RT}{R_{ct}F} \qquad (43)$$

Where R is the universal gas constant (8.314 $JK^{-1}mol^{-1}$), F is Faraday constant (96486 C mol^{-1}) and T is the temperature (298.15 K) and R_{ct} is the charge transfer resistance (Ω). R_s is the solution resistance which takes into effect at the interface between the surface of the GCE and the electrolyte. The exchange current density of $LiMn_2O_4$ at 0.46 V was 8.07×10^{-5} A cm^{-2}, which corresponds to a slow rate of electron transfer due to the poor catalytic effect of pristine $LiMn_2O_4$. The i_o of the modified cathode material is significantly higher than the pristine material which indicates improved catalytic activity of the novel cathode material.

From Table 6 above, the decrease of R_{ct} at lower voltages indicates that the electrochemical polarization decreases, which is beneficial to the transfer of Li^+. The interfacial capacitance value (C_{dl}) of $LiMn_2O_4$ was similar than that of modified samples, indicating that the $LiMn_2O_4$ electrode has a similar surface area which redox reactions take place and the intercalation/deintercalation of li-ions.

Chapter 6: Conclusion

Lithium ion transition metal oxides as cathode materials for batteries have received much attention as battery cathode materials ever since the invention of new age technology applications such as laptops, cellphones and electric vehicles. $LiMn_2O_4$ forms part of a collection of intercalation cathode materials in which li-ions intercalate between the cathode and anode. Of these intercalation cathodes, $LiCoO_2$ is mostly industrialized as it is easier to synthesize and displays a superior theoretical capacity in comparison to that of $LiMn_2O_4$ and $LiNiO_2$. $LiCoO_2$ is however very costly and not environmentally friendly, hence the decision to study the capacitive dynamics of modified $LiMn_2O_4$. In this study, the properties of $LiMn_2O_4$ were, investigated and the modification thereof by forming a coated composite cathode material comprising of $LiMn_2O_4$, AlF_3, and rGO which gives rise to the novel [$AlF_3LiMn_2O_4$-rGO].

The novel cathode material was successfully synthesized and analysed using various electrochemical and spectroscopy analysis techniques. From the characterized materials, I am

confident that the novel cathode material obtained will provide immense improvements to the capacity and energy density of the cathode. Improvements in structural and electrochemical stability due to the addition of AlF_3 and rGO to the pristine $LiMn_2O_4$ was confirmed. This is due to the fact that the material will be able to undergo more charge/discharge cycles before degradation and capacity loss as compared to the pristine $LiMn_2O_4$ cathode. This can be observed from XRD and TEM crystallinity determinations of the novel material as well as the interlayer d-spacings (d = 0.187 nm). The cathode material will therefore have the ability to withstand an improved number of charge/discharge cycles before losing its intrinsic properties in lithium ion battery applications. The electrochemical parameters of the modified $LiMn_2O_4$ improved substantially. The current conducting capacity improved by about 5 times as can be seen when comparing the current densities in the cyclic voltammograms in Figure 25 where of Ipa/Ipa 2.89 µA and -2.08 µA compared to Figure 27 with Ipa/Ipc of 10.14 µA and -7.17 µA respectively. The good capacitive properties of the material was also confirmed through electrochemical impedance studies where the absence of the semi-circle region on the nyquist plot as well as a substantial reduction in charge transfer resistance of 318 to 245.70 Ω was reported. The determination of these parameters clearly indicate that a capacity enhancement will be observed when applying the novel [$AlF_3LiMn_2O_4$-rGO] cathode material to a battery or coin cell.

Chapter 7: Recommendations for Future Work

- Coin cells will be fabricated in order to determine the exact electrochemical properties of the material including cyclability and rate capability.
- The incorporation of Nuclear magnetic resonance (NMR) studies into my work in order to compare the quadrupolar interactions between the Li, Al and F nuclei as well as to determine the isotropic nature of the pristine and novel cathode materials.
- This aspect of the study included to coating of $LiMn_2O_4$, but the doping of the $LiMn_2O_4$ cathode material with various dopants and doing a comparative study between the cathode modification techniques.

Chapter 8: References

[1] United Nation, "Our Common Future, Chapter 2: Towards Sustainable Development - A/42/427 Annex, Chapter 2 - UN Documents: Gathering a body of global agreements," *UN Documents*. 1987.

[2] N. Armaroli and V. Balzani, "Towards an electricity-powered world," *Energy Environ. Sci.*, vol. 4, no. 9, p. 3193, 2011.

[3] D. Streimikiene, R. Ciegis, and D. Grundey, "Energy indicators for sustainable development in Baltic States," *Renew. Sustain. Energy Rev.*, vol. 11, no. 5, pp. 877–893, 2007.

[4] K. Zaghib, P. Charest, A. Guerfi, J. Shim, M. Perrier, and K. Striebel, "LiFePO4 safe Li-ion polymer batteries for clean environment," vol. 146, pp. 380–385, 2005.

[5] J. A. Herron, J. Kim, A. A. Upadhye, G. W. Huber, and C. T. Maravelias, "A general framework for the assessment of solar fuel technologies," *Energy Environ. Sci.*, vol. 8, no. 1, pp. 126–157, 2015.

[6] A. Sternberg and A. Bardow, "Power-to-What? – Environmental assessment of energy storage systems," *Energy Environ. Sci.*, vol. 8, no. 2, pp. 389–400, 2015.

[7] X. Zhang, K. Rajagopalan, H. Lei, R. Ruan, and B. K. Sharma, "An overview of a novel concept in biomass pyrolysis: microwave irradiation," *Sustain. Energy Fuels*, vol. 1, pp. 1664–1699, 2017.

[8] T. Linden, David, Reddy, McGraw-Hill, New York, *Handbook of batteries*, pp 1020-1140, 2004.

[9] J. B. Goodenough, "Basic Research Needs for Electrical Energy Storage," *Off. Basic Energy Sci. Dep. Energy*, p. 186, 2007.

[10] "World batteries. (2017, January 23). Retrieved from http://www.freedoniagroup.com/industry-study/world-batteries-2939.htm." 2017.

[11] Z. Piero, " Inorganic electrochemistry: Theory practise and application," *Royal society of chem.,*pp. 49-111, 2003

[12]   M. Winter and R. J. Brodd, "What are batteries, fuel cells, and supercapacitors?," *Chem. Rev.*, vol. 104, no. 10, pp. 4245–4269, 2004.

[13]   S. Curtin and J. Gangi, "Fuel Cell Technologies Market Report 2015," *Https://Energy.Gov/Sites/Prod/Files/2016/10/F33/Fcto_2015_Market_Report.Pdf*, p. 60, 2015.

[14]   M. Armand and J.-M. Tarascon, "Building better batteries," *Nature*, vol. 451, no. 7179, pp. 652–657, 2008.

[15]   N. West, K. I. Ozoemena, C. O. Ikpo, P. G. L. Baker, and E. I. Iwuoha, "Transition metal alloy-modulated lithium manganese oxide nanosystem for energy storage in lithium-ion battery cathodes," *Electrochim. Acta*, vol. 101, pp. 86–92, 2013.

[16]   M. Srivastava, J. Singh, T. Kuila, R. K. Layek, N. H. Kim, and J. H. Lee, "Recent advances in graphene and its metal-oxide hybrid nanostructured for lithium-ion batteries," *Nanoscale*, vol. 7, no. 7, pp. 4820–4868, 2015.

[17]   P. G. Bruce, B. Scrosati, and J. Tarascon, "Lithium Batteries Nanomaterials for Rechargeable Lithium Batteries ** Angewandte," pp. 2930–2946, 2008.

[18]   Y. Wu, R. Zhao, H. Zhou, D. Zhang, and W. Zhao, "Synthesis and application of a novel Cu / RGO @ Pb alloy for lead-acid batteries," *Electrochim. Acta*, vol. 222, pp. 116–122, 2016.

[19]   H.-W. Chan, J.G. Duh, S.R. Sheen, S.Y. Tsai, and C.R. Lee, "New surface modified material for $LiMn_2O_4$ cathode material in Li-ion battery," *Surf. Coatings Technol.*, vol. 200, no. 5–6, pp. 1330–1334, 2005.

[20]   Q. Liu, S. Wang, H. Tan, Z. Yang, and J. Zeng, "Preparation and doping mode of doped $LiMn_2O_4$ for Li-ion batteries," *Energies*, vol. 6, no. 3, pp. 1718–1730, 2013.

[21]   J. Cho, S. Jeong, and Y. Kim, "Commercial and research battery technologies for electrical energy storage applications," *Prog. Energy Combust. Sci.*, vol. 48, pp. 84–101, 2015.

[22]   Q. Long *et al.*, "Improving the cycle life of lead-acid batteries using three-dimensional reduced graphene oxide under the high-rate partial-state-of-charge condition," *J. Power*

68

Sources, vol. 343, pp. 188–196, 2017.

[23]   D. Berndt, "Electrochemical Energy Storage," *Handb. Batter. 2nd Ed.*, vol. 2, 2003.

[24]   S. Zhang, H. Zhang, J. Cheng, W. Zhang, G. Cao, and H. Zhao, "Novel polymer-graphite composite grid as a negative current collector for lead-acid batteries," *J. Power Sources*, vol. 334, pp. 31–38, 2016.

[25]   P. Bauer, Library congress, Washington, *Batteries for space power systems*, NASA, pp. 90-120, 1969.

[26]   Y. Wang and G. Cao, "Developments in nanostructured cathode materials for high-performance lithium-ion batteries," *Adv. Mater.*, vol. 20, no. 12, pp. 2251–2269, 2008.

[27]   R. S. Treptow, "Lithium Batteries: A Practical Application of Chemical Principles," *J. Chem. Educ.*, vol. 80, no. 9, p. 1015, 2003.

[28]   M. C. Rao, "LiMn$_2$O$_4$ Cathodes for solid state lithium-ion batteries - energy storage and conversion," *J. Optoelectron. Biomed. Mater.*, vol. 5, no. 1, pp. 9–16, 2013.

[29]   H. K. Liu, "An overview—Functional nanomaterials for lithium rechargeable batteries, supercapacitors, hydrogen storage, and fuel cells," *Mater. Res. Bull.*, vol. 48, no. 12, pp. 4968–4973, 2013.

[30]   Y. Zhang *et al.*, "CoO/Co$_3$O$_4$/graphene nanocomposites as anode materials for lithium-ion batteries," *J. Alloys Compd.*, vol. 699, pp. 672–678, 2017.

[31]   H. Cai, K. Han, H. Jiang, J. Wang, and H. Liu, "Self-standing silicon-carbon nanotube/graphene by a scalable in situ approach from low-cost Al-Si alloy powder for lithium ion batteries," *J. Phys. Chem. Solids*, vol. 109, pp. 9–17, 2017.

[32]   G. W. Zhou *et al.*, "Facile spray drying route for the three-dimensional graphene-encapsulated Fe$_2$O$_3$ nanoparticles for lithium ion battery anodes," *Ind. Eng. Chem. Res.*, vol. 52, no. 3, pp. 1197–1204, 2013.

[33]   G. Kucinskis, G. Bajars, and J. Kleperis, "Graphene in lithium ion battery cathode materials: A review," *J. Power Sources*, vol. 240, pp. 66–79, 2013.

[34]   C. Zhang, X. Liu, Q. Su, J. Wu, T. Huang, and A. Yu, "Enhancing Electrochemical

Performance of LiMn$_2$O$_4$ Cathode Material at Elevated Temperature by Uniform Nanosized TiO$_2$ Coating," *ACS Sustain. Chem. Eng.*, vol. 5, no. 1, pp. 640–647, 2017.

[35]   J. Pröll *et al.*, "Comparative studies of laser annealing technique and furnace annealing by X-ray diffraction and Raman analysis of lithium manganese oxide thin films for lithium-ion batteries," *Thin Solid Films*, vol. 531, pp. 160–171, 2013.

[36]   G. W. Ling *et al.*, "Structural and thermal stabilities of spinel LiMn$_2$O$_4$ materials under commercial power batteries cycling and abusive conditions," *Int. J. Electrochem. Sci.*, vol. 7, no. 3, pp. 2455–2467, 2012.

[37]   A. Tron, Y. D. Park, and J. Mun, "AlF$_3$-coated LiMn$_2$O$_4$ as cathode material for aqueous rechargeable lithium battery with improved cycling stability," *J. Power Sources*, vol. 325, pp. 360–364, 2016.

[38]   M. Hu, X. Pang, and Z. Zhou, "Recent progress in high-voltage lithium ion batteries," *J. Power Sources*, vol. 237, no. September 2013, pp. 229–242, 2013.

[39]   M. S. Whittingham, "Lithium batteries and cathode materials," *Chem. Rev.*, vol. 104, no. 10, pp. 4271–4301, 2004.

[40]   M. Nakayama, S. Yamada, R. Jalem, and T. Kasuga, "Density functional studies of olivine-type LiFePO$_4$ and NaFePO$_4$ as positive electrode materials for rechargeable lithium and sodium ion batteries," *Solid State Ionics*, vol. 286, pp. 40–44, 2016.

[41]   D. Di Lecce, R. Verrelli, and J. Hassoun, "New lithium ion batteries exploiting conversion/alloying anode and LiFe$_{0.25}$Mn$_{0.5}$Co$_{0.25}$PO$_4$ olivine cathode," *Electrochim. Acta*, vol. 220, pp. 384–390, 2016.

[42]   J. B. Padhi, A. K.; Nanjundaswamy, K Goodenough, "Phospho-olivines as Positive-Electrode Materials for Rechargeable Lithium Batteries," *J. Electrochem. Soc.*, vol. 144, no. 4, pp. 1–7, 1997.

[43]   C.C. Yang, J.H. Jang, and J.R. Jiang, "Comparison Electrochemical Performances of Spherical LiFePO$_4$/C Cathode Materials at Low and High Temperatures," *Energy Procedia*, vol. 61, pp. 1402–1409, 2014.

[44] R. Verrelli and J. Hassoun, "High capacity tin-iron oxide-carbon nanostructured anode for advanced lithium ion battery," *J. Power Sources*, vol. 299, pp. 611–616, 2015.

[45] J. B. Goodenough and Y. Kim, "Challenges for rechargeable batteries," *J. Power Sources*, vol. 196, no. 16, pp. 6688–6694, 2011.

[46] O. K. Park, Y. Cho, S. Lee, H.C. Yoo, H.K. Song, and J. Cho, "Who will drive electric vehicles, olivine or spinel?," *Energy Environ. Sci.*, vol. 4, no. 5, p. 1621, 2011.

[47] G. Xu, Z. Liu, C. Zhang, G. Cui, and L. Chen, "Strategies for improving the cyclability and thermo-stability of LiMn2O4 -based batteries at elevated temperatures," *J. Mater. Chem. A*, vol. 3, no. 8, pp. 4092–4123, 2015.

[48] J. Li, X. He, and R. Zhao, "Electrochemical performance of SrF_2-coated $LiMn_2O_4$ cathode material for Li-ion batteries," *Trans. Nonferrous Met. Soc. China*, vol. 17, no. 6, pp. 1324–1327, 2007.

[49] K. S. Novoselov *et al.*, "Electric Field Effect in Atomically Thin Carbon Films," *Science*, vol. 306, no. 5696, pp. 666–669, 2004.

[50] V. Singh, D. Joung, L. Zhai, S. Das, S. I. Khondaker, and S. Seal, "Graphene based materials: Past, present and future," *Prog. Mater. Sci.*, vol. 56, no. 8, pp. 1178–1271, 2011.

[51] D. Zhou, W.L. Song, X. Li, L.Z. Fan, and Y. Deng, "Tin nanoparticles embedded in porous N-doped graphene-like carbon network as high-performance anode material for lithium-ion batteries," *J. Alloys Compd.*, vol. 699, pp. 730–737, 2017.

[52] J. C. Slonczewski and P.R. Weiss, "Band structure of graphite," *Physical Review*, vol. 109, no. 2. pp. 272–279, 1958.

[53] C. Lee, X. Wei, J. W. Kysar, and J. Hone, "Measurement of the Elastic Properties and Intrinsic Strength of Monolayer Graphene," *Science*, vol. 321, no. 5887, pp. 385–388, 2008.

[54] R.F. Kroto, H.W. Heath, J.R. O'Brian, S.C. Curl, "C60- Buckminsterfullerene," *Nature*, vol. 318, pp. 162–163, 1985.

[55] Y. Liu *et al.*, "Surfactant-templating strategy for ultrathin mesoporous TiO2 coating on flexible graphitized carbon supports for high-performance lithium-ion battery," *Nano*

Energy, vol. 25, pp. 80–90, 2016.

[56]   H. Wang *et al.*, "Rechargeable Li–O2 batteries with a covalently coupled $MnCo_2O_4$–graphene hybrid as an oxygen cathode catalyst," *Energy Environ. Sci.*, vol. 5, no. 7, p. 7931, 2012.

[57]   D. Zuo, G. Tian, X. Li, D. Chen, and K. Shu, "Recent progress in surface coating of cathode materials for lithium ion secondary batteries," *J. Alloys Compd.*, vol. 706, pp. 24–40, 2017.

[58]   X. Fang, M. Ge, J. Rong, and C. Zhou, "Graphene-oxide-coated $LiNi_{0.5}Mn_{1.5}O_4$ as high voltage cathode for lithium ion batteries with high energy density and long cycle life," *J. Mater. Chem. A*, vol. 1, no. 12, p. 4083, 2013.

[59]   Q. Wu, Y. Yin, S. Sun, X. Zhang, N. Wan, and Y. Bai, "Novel AlF_3 surface modified spinel $LiMn_{1.5}Ni_{0.5}O_4$ for lithium-ion batteries: Performance characterization and mechanism exploration," *Electrochim. Acta*, vol. 158, pp. 73–80, 2015.

[60]   W. Kleist, C. Haeßner, O. Storcheva, and K. Köhler, "A simple aqueous phase synthesis of high surface area aluminum fluoride and its bulk and surface structure," *Inorganica Chim. Acta*, vol. 359, no. 15, pp. 4851–4854, 2006.

[61]   H. Liu and D. Tang, "The Effect of Nanolayer AlF_3 Coating on $LiMn_2O_4$ Cycle Life in High Temperature for Lithium Secondary Batteries 1," vol. 45, no. 7, pp. 817–819, 2009.

[62]   B.C. Park *et al.*, "Improvement of structural and electrochemical properties of AlF3-coated $Li[Ni_{1/3}Co_{1/3}Mn1/3]O_2$ cathode materials on high voltage region," *J. Power Sources*, vol. 178, no. 2, pp. 826–831, 2008.

[63]   D.L. Gerrard, "Raman Spectroscopy," *Anal. Chem.*, vol. 66, no. 12, pp. 547–557, 1994.

[64]   R. D. Alves, L.C. Rodrigues, J.R. Andrade, M. Fernandes, J.V. Pinto, L. Pereira, A. Pawlicka, R. Martins, E. Fortunato, *et al.*, "GelatinnZn(CF3SO3)2 polymer electrolytes for electrochromic devices," *Electroanalysis*, vol. 25, no. 6, pp. 1483–1490, 2013.

[65]   D.D. MacDonald, "Reflections on the history of electrochemical impedance spectroscopy," *Electrochim. Acta*, vol. 51, no. 8–9, pp. 1376–1388, 2006.

[66]   P.G.M. Pacios, I. Martín-Fernández, R. Villa, E.M. De Valle, "Carbon Nanotubes as

Suitable Electrochemical Platforms for Metalloprotein Sensors and Genosensors," *Intech*, pp. 299-323, 2011.

[67]   Z. Yang, Q. Zheng, H. Qiu, J. Li, and J. Yang, "A simple method for the reduction of graphene oxide by sodium borohydride with $CaCl_2$ as a catalyst," *New Carbon Mater.*, vol. 30, no. 1, pp. 41–47, 2015.

[68]   N. Murali, S. J. Margarette, and V. Veeraiah, "Structural, Microstructural and Raman spectral studies of LiMn $_{2-x}$ Zn $_x$ O $_4$ (x = 0.02, 0.12 and 0.22) for Lithium-ion batteries," *IOP Conf. Ser. Mater. Sci. Eng.*, vol. 149, p. 12193, 2016.

[69]   T. N. Renata Lewandowska, Miyoko Okada, "Raman Spectroscopy Applied to the Lithium-ion Battery Analysis," *Horiba Sci.*, no. figure 2, pp. 3–4, 2001.

[70]   Y. Ding, J. Xie, G. Cao, T. Zhu, and H. Yu, "Single-Crystalline $LiMn_2O_4$ Nanotubes Synthesized Via Template-Engaged Reaction as Cathodes for High-Power Lithium Ion Batteries," *Adv. Mater.*, pp. 348–355, 2011.

[71]   Y. L. Ding, J. Xie, G. S. Cao, T. J. Zhu, H. M. Yu, and X. B. Zhao, "Enhanced Elevated-Temperature Performance of Al-Doped Single-Crystalline $LiMn_2O_4$ Nanotubes as Cathodes for Lithium Ion Batteries," *Phys. Chem.,* vol. 115, no. 19, pp. 9821–9825, 2011.

[72]   V. I. Torgashev *et al.*, "Magnetic and dielectric response of cobalt-chromium spinel $CoCr_2O_4$ in the terahertz frequency range," *Phys. Solid State*, vol. 54, no. 2, pp. 350–359, 2012.

[73]   A. R. Naghash and J. Y. Lee, "Preparation of spinel lithium manganese oxide by aqueous," *Power sources*, vol. 84, no. 2, pp. 284–293, 2000.

[74]   C. W. Dunnill and D. H. Gregory, "Studies on chromium / aluminium-doped manganese spinel as cathode materials for lithium-ion batteries — A novel chelated sol – gel synthesis," *Mater. processing tech.,* vol. 8, no. 1-3, pp. 520–531, 2008.

[75]   N. Ross, M. Nzaba, W. Ntuthuko, C. Ikpo, P. Baker, and E. Iwuoha, "Palladium-Gold Nanoalloy Surface Modified $LiMn_2O_4$ Cathode for Enhanced Li-Ion Battery," *Nanomaterials*, pp 1-6, 2015.

73

[76] K. Hariprasad, N. Naresh, B. Nageswara Rao, M. Venkateswarlu, and N. Satyanarayana, "Preparation of LiMn$_2$O$_4$ Nanorods and Nanoparticles for Lithium-ion Battery Applications," *Mater. Today Proc.*, vol. 3, no. 10, pp. 4040–4045, 2016.

[77] S. M. Coman *et al.*, "NbF$_5$–AlF$_3$ Catalysts: Design, Synthesis, and Application in Lactic Acid Synthesis from Cellulose," *ACS Catal.*, vol. 5, no. 5, pp. 3013–3026, 2015.

[78] K. Roodenko, M. D. Halls, Y. Gogte, O. Seitz, J. F. Veyan, and Y. J. Chabal, "Nature of hydrophilic aluminum fluoride and oxyaluminum fluoride surfaces resulting from XeF$_2$ treatment of Al and Al$_2$O$_3$," *J. Phys. Chem. C*, vol. 115, no. 43, pp. 21351–21357, 2011.

[79] B. Chen, Wufeng; Yang, Lifeng; Prakiti, "Preparation of graphene by the rapid and mild thermal reduction of graphene oxide induced by microwaves," *Technol. Chem.*, vol. 48, no.4, pp. 1146-1152, 2010.

[80] C. Ouyang, S. Shi, Z. Wang, X. Huang, and L. Chen, "Experimental and theoretical studies on dynamic properties of Li ions in LixMn2O4," *Solid State Commun.*, vol. 130, no. 7, pp. 501–506, 2004.

[81] Z. Cao and B. Wei, "Fragmented carbon nanotube macrofilms as adhesive conductors for lithium-ion batteries," *ACS Nano*, vol. 8, no. 3, pp. 3049–3059, 2014.